J. Fluid Mech. (2006), *vol.* 553, *pp.* 283–322.
doi:10.1017/S0022112006008883 Printed in the United Kingdom

Short-wavelength instability and decay of a vortex pair in a stratified fluid

By KEIKO K. NOMURA, HIDEAKI TSUTSUI, DANIEL MAHONEY AND JAMES W. ROTTMAN

Department of Mechanical and Aerospace Engineering, University of California, San Diego, La Jolla, CA 92093-0411, USA

(Received 12 August 2004 and in revised form 31 October 2005)

The evolution of a counter-rotating vortex pair in a stably stratified fluid is investigated using direct numerical simulations. The study focuses on the short-wavelength elliptic instability occurring in this flow and the subsequent decay of the vortices. Depending on the level of stratification, as characterized by the Froude number which indicates the time scale of buoyancy to that of the instability, and the stage of evolution, stratification effects may significantly alter the behaviour of the flow. In the case of weak to moderate stratification, the elliptic instability develops qualitatively in the same manner as in unstratified fluid. The primary effect of stratification is to reduce the vortex separation distance which enhances the mutually induced strain. Consequently, the instability has an earlier onset and higher growth rate with increasing stratification. The behaviour is essentially described by linear stability theory for unstratified flow if the varying separation distance is taken into account. On the other hand, the final breakdown and decay of the flow may be greatly modified by stratification since buoyancy effects eventually emerge after sufficient time has elapsed. The decay is enhanced owing to additional mechanisms not present in unstratified flow. Secondary vertical vortex structures form between the primary vortices promoting fluid exchange in the transverse direction. Detrainment of fluid from the primary vortices by the generated baroclinic torque also contributes to the more rapid breakdown of the flow. In the case of strong stratification, in which the time scale of buoyancy is comparable to that of the instability, the flow is significantly altered. As a result of strong baroclinic torque, the primary vortices are brought together and detrainment occurs earlier. The associated reduction in radii of the vortices results in a higher axial wave mode and a more complex radial structure of the instability. Detrainment and mixing accelerate their decay. Late time evolution is dominated by the successive generation of alternate signed baroclinic torque which results in an oscillation of the total flow circulation at the buoyancy frequency.

1. Introduction

A counter-rotating vortex pair is a model flow of both practical and fundamental significance. Such a flow may occur in the wake of an aircraft and can be hazardous to following aircraft (Spalart 1998). Knowledge of the rate of decay of these vortices which includes the effects of atmospheric conditions such as density stratification and turbulence is critical for air traffic control. More relevant to the present study is the fundamental interest in elementary vortex flows; the knowledge of which is prerequisite for understanding the interaction and behaviour of vortices in more complex flows.

For example, in fully developed turbulence, coherent vortex structures are found to occur at small scales (She, Jackson & Orszag 1991; Jimenez *et al.* 1993; Nomura & Post 1998) and may play a significant role in the dynamics and statistical properties of the flow. In stably stratified turbulence, counter-rotating vortices can generate overturns with regions of high diapycnal mixing in between them (Diamessis & Nomura 2004). Accordingly, it is of interest to determine what effect stratification has on these vortices.

In an unstratified fluid, a pair of counter-rotating parallel vortices is known to exhibit two types of (three-dimensional) instabilities, a long-wavelength and a short-wavelength instability. The long-wavelength (Crow) instability (Crow 1970) results in a symmetric sinusoidal deformation of the vortex cores. According to Crow's linear stability theory, the wavelength with the maximum growth rate depends on the vortex dipole aspect ratio, defined in this case as the ratio of the vortex core radius r_c to the initial vortex separation distance b_0. For a Rankine vortex with $r_c/b_0 = 0.0985$ (presumed characteristic of aircraft trailing wing vortices), Crow calculated that this most amplified wavelength is approximately $8.6b_0$. According to Han *et al.* (2000), laboratory experiments, numerical simulations and field measurements have found that for aircraft trailing wing vortices, the most amplified wavelength is in the range $5b_0$ to $10b_0$. The variation about the expected value is attributed to differences in r_c/b_0 and vorticity distribution in the various studies, and the effects of ambient turbulence in the atmospheric observations. Detailed studies have shown that the Crow instability leads to vortex reconnection and the formation of vortex rings which may persist for long times (Leweke & Williamson 1998*a*, *b*).

A short-wavelength instability has also been observed in both laboratory experiments (Sarpkaya & Suthon 1991; Thomas & Auerbach 1994; Leweke & Williamson 1998*a*) and numerical simulations (Orlandi *et al.* 1998; Laporte & Corjon 2000). Leweke & Williamson 1998*a*, here in after referred to as LW98) identified the instability as a *cooperative elliptic* instability associated with the ellipticity of the streamlines in the vortex cores owing to the strain induced by one vortex on the other (Tsai & Widnall 1976; Waleffe 1990). An antisymmetric sinusoidal deformation of the cores is observed. Experimental studies report a range of wavelengths $0.6b_0$ to $0.8b_0$ (Thomas & Auerbach 1994; LW98). A stability analysis of the Lamb–Chaplygin vortex pair performed by Billant, Brancher & Chomaz (1999) showed the existence of both symmetric and antisymmetric short-wavelength instabilities, the latter exhibiting higher growth rates. Sipp & Jacquin (2003) showed that the growth rates depend on the dipole aspect ratio and the preference for the antisymmetric mode increases with increasing aspect ratio. They also considered the effects of viscosity which damp the perturbation growth rate and also increase the vortex radii and hence, the aspect ratio (see § 3.3.3). The predicted growth rate is in good agreement with the experiments of LW98. In the later stages of flow development, the short-wave instability gives rise to secondary transverse vortex structures which lead to rapid vortex decay and transition to turbulence (LW98; Laporte & Corjon 2000).

The interaction of the Crow and short-wavelength instabilities has also been considered (LW98; Laporte & Corjon 2000). The behaviour of the flow is found to depend on the relative significance of the initial energy of each instability mode (Laporte & Corjon 2000). When the Crow instability dominates, the short-wave instability is locally enhanced where the deformation of the Crow instability brings the vortices close together. This is due to the increase in mutually induced strain as the separation distance decreases (LW98). Long-term evolution is sensitive to both instabilities (Laporte & Corjon 2000).

The effects of stable density stratification on two-dimensional vortex pairs have been considered in a number of studies (Scorer & Davenport 1970; Crow 1974; Spalart 1996). In an unstratified fluid, a two-dimensional counter-rotating vortex pair descends, owing to its mutually induced velocity, at a constant speed while maintaining a constant separation distance. Results from these studies indicate that ambient stratification with $Fr \geqslant 1$, where $Fr = W_0/Nb_0$, and W_0 is the initial advection velocity and N is the buoyancy frequency, causes a decrease in separation distance and subsequent acceleration of vertical motion. This disagrees with experimental observations (Sarpkaya 1983; Delisi & Robins 2000) and three-dimensional simulations (Robins & Delisi 1998; Garten *et al.* 2001) which indicate a simultaneous decrease in separation distance and deceleration. A two-dimensional analysis by Holzäpfel & Gerz (1999) shows early deceleration followed by acceleration. It was suggested that the acceleration phase is not observed in actual flows since beyond the early phase, the dynamics are dominated by three-dimensional instabilities. As the vortices descend in a stratified fluid, opposite signed vorticity is generated through baroclinic torque (see figure 8). The associated flow drives the vortices towards each other (Spalart 1996). As shown by Holzäpfel & Gerz (1999), the induced velocity field of the baroclinic torque also causes a reduced descent speed and detrainment of fluid from the vortex pair oval.

The effect of ambient stratification on the Crow instability has been investigated using numerical simulations (Robins & Delisi 1998; Garten *et al.* 2001). Robins & Delisi (1998) find that increasing stratification accelerates linking and ring formation. For strong stratification ($Fr \leqslant 2$), the formation of rings is suppressed and instead, 'puffs' are formed. Garten *et al.* (2001) find a critical Froude number, $Fr_{cr} \approx 2/3$, such that for $Fr > Fr_{cr}$, the reduced separation distance results in a faster growth of the Crow instability. For $Fr < Fr_{cr}$, the separation distance increases, retarding instability growth and preventing significant vortex reconnection to occur. The symmetry boundary conditions used in the transverse direction precluded the development of any antisymmetric instabilities in their simulations.

An experimental and numerical study by Delisi & Robins (2000) reported the development of a short-wavelength instability in stably stratified fluid. The circulation Reynolds number, $Re_\Gamma = \Gamma/\nu$ where Γ is the vortex circulation and ν is the kinematic viscosity, is 24 000 in the experiments and 1465 in the simulations, and the Fr values are $0.73 \leqslant Fr \leqslant 1.1$. The wavelength of the instability is longer (approximately b_0 to $2b_0$) than that observed in the unstratified flows ($\leqslant b_0$). The instability also exhibits an earlier onset and a more rapid growth, apparently at the expense of the Crow instability. Results from large-eddy simulations (LES) of vortex pairs in stably stratified fluid at high Re_Γ ($Re_\Gamma \sim 10^7$) (Switzer & Proctor 2000) indicate that the level of ambient stratification and turbulence determine whether the long-wave or short-wave instability dominates. Holzäpfel, Gerz & Baumann (2001) performed LES for $Re_\Gamma = 7400$ and report that in the case of a quiescent atmosphere and stratification levels $1 \leqslant Fr \lesssim 3$, the decay of the vortices is controlled by the interaction of the short-wave instability and baroclinic vorticity. Increasing stratification accelerates the short-wave instability which they suggest is due to the reduced vortex spacing. Intense vertical vortex structures are induced by baroclinic torque. These structures result in lateral transport and turbulent mixing of the primary vorticity which promotes a rapid decay of the vortex pair.

These previous studies indicate that a short-wavelength instability occurs in stably stratified flows and that it can dominate with significant stratification. There is also an enhancement of the instability with increasing levels of stratification. However,

quantitative assessment of the instability is limited. Growth rates have not been evaluated and the variation in wavelength has not been verified. In general, it has not been clearly established whether the observed instability in the stratified flows is the cooperative elliptic instability occurring in unstratified flow (Delisi & Robins 2000). At present, there are no corresponding three-dimensional linear stability analyses for the stratified flow.

The objective of the present study is to investigate further the short-wavelength instability and subsequent decay of a vortex pair in a stably stratified fluid using direct numerical simulation. Here, we consider only the short-wave instability by restricting the development of the Crow instability in the simulations. The Reynolds number Re_Γ is fixed at a value comparable to the experiments of LW98 and we consider a greater range of stratification levels ($1 \leqslant Fr \leqslant 10$, $Fr = \infty$) than in previous studies. A more thorough and quantitative assessment of the instability and influence of stratification is performed. Details of the instability, not provided in previous studies, are examined and compared with those of unstratified flow. Growth rates are evaluated. Energy spectra are computed and show the evolution of the primary instability, development of harmonics, and late-time behaviour. Detailed analysis is carried out in order to understand the development of structural features and the physical mechanisms involved in the decay of the vortex pair.

The results provide a more comprehensive description of the effects of stable stratification in this flow. Depending on Fr, which indicates the time scale of buoyancy to that of the instability, and the stage of evolution, stratification effects may significantly alter the behaviour of the flow. For weak to moderately stratified flows ($\infty > Fr \geqslant 2$), the time scale of buoyancy is relatively large. Thus, at early times when the instability develops, stratification results only in a variation of the unstratified flow (decreasing separation distance) and the behaviour of the instability is essentially described by linear theory for unstratified flow with appropriate scaling. On the other hand, the final breakdown and decay of the flow may be greatly modified by stratification since buoyancy effects eventually emerge after sufficient time has elapsed. For strongly stratified flow, $Fr \sim 1$, the time scales of the instability and stratification are comparable and the associated processes interact significantly. We consider $Fr \sim 1$ to be a limit for our analysis of the short-wavelength instability, corresponding to a transition between convective dominated and stratification dominated flow. The two-dimensional base flow is significantly altered and the instability does not develop in the same manner, or to the extent, as in the weak to moderately stratified flows. We note that very strongly stratified flows, $Fr < 1$, exhibit different behaviour and the elliptic instability is not expected to be realized. These flows are outside the main scope of this study.

The numerical simulations are described in § 2. Results are presented in § 3: the overall behaviour of the flows is first described and details of the (linear) instability and (nonlinear) late-time decay are then presented and discussed. Conclusions are given in § 4.

2. Direct numerical simulations

Direct numerical simulations of a counter-rotating vortex pair in an initially uniform stably stratified fluid are performed for this study. Figure 1 shows the initial flow geometry and the coordinate system. Here, the spatial coordinates, x, y, z, correspond to the transverse, axial and vertical directions, respectively.

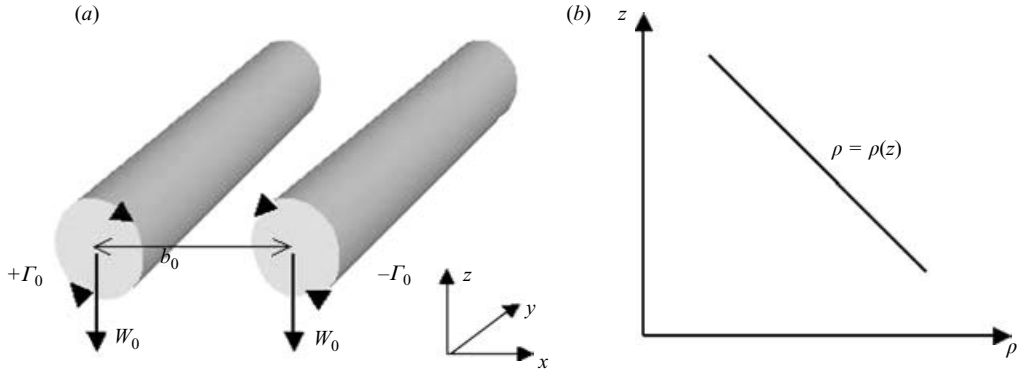

FIGURE 1. Coordinate system and initial conditions for counter-rotating vortex pair and uniform stable stratification. (*a*) Initial vortices of circulation, $\pm\Gamma_0$, with centres separated by a distance, b_0, moving with downward induced velocity, $W_0 = \Gamma_0/2\pi b_0$. (*b*) Background linear density profile $\overline{\rho}(z)$.

The governing equations with the Boussinesq approximation are:

$$\nabla \cdot \boldsymbol{v} = 0, \tag{2.1}$$

$$\frac{\partial \boldsymbol{v}}{\partial t} + \boldsymbol{v} \cdot \nabla \boldsymbol{v} = -\frac{1}{\rho_0}\nabla p + \nu \nabla^2 \boldsymbol{v} - \alpha_T T \boldsymbol{g}, \tag{2.2}$$

$$\frac{\partial T}{\partial t} + \boldsymbol{v} \cdot \nabla(\overline{T}(z) + T) = \kappa \nabla^2 T, \tag{2.3}$$

where ρ_0 is a constant reference density, ν is the kinematic viscosity, $\boldsymbol{g} = (0, 0, -g)$ is the acceleration due to gravity, and κ is the thermal diffusivity. In the above equations, $\boldsymbol{v} = (u, v, w)$ is the instantaneous velocity, p is the deviation of the pressure from its hydrostatic value and T is the deviation of the temperature from the background temperature, i.e. the instantaneous temperature is $\widetilde{T} = T_0 + \overline{T}(z) + T(x, y, z, t)$, where $\overline{T}(z)$ is the imposed background temperature. The volumetric expansion coefficient, α_T, is defined as, $\alpha_T = -(1/\rho_0)(\partial\widetilde{\rho}/\partial\widetilde{T})$. The corresponding density field is $\widetilde{\rho} = \rho_0 + \overline{\rho}(z) + \rho(x, y, z, t)$, where the imposed uniform stable stratification corresponds to $\mathrm{d}\overline{\rho}/\mathrm{d}z$.

The initial base flow consists of a pair of two-dimensional counter-rotating vortices. The flow is represented by a superposition of two Lamb–Oseen vortices which was found to fit well the experimental data of LW98. The corresponding vorticity distribution is given by,

$$\omega_y(x, z, t_0) = \Omega_0 \exp\left(\frac{-((x - x_1)^2 + (z - z_1)^2)}{a_0^2}\right) - \Omega_0 \exp\left(\frac{-((x - x_2)^2 + (z - z_2)^2)}{a_0^2}\right), \tag{2.4}$$

where $\Omega_0 = \Gamma/\pi a_0^2$ is the peak vorticity, a_0 is the initial value of the vortex radius and (x_1, z_1) and (x_2, z_2) are the initial coordinates of the two vortex centroids ($z_1 = z_2$). Note that here, the vortex radius is based on the vorticity polar moment and given by $a^2 = \langle r^2\omega_y\rangle/\langle\omega_y\rangle$, where r is the radial distance from a vortex centroid and $\langle\rangle$ indicates an area average in $x - z$. The intial separation distance is $b_0 = |x_1 - x_2|$. The vortex dipole aspect ratio for all simulations performed here is $a_0/b_0 = 0.177$. This is comparable to the estimated value $a_0/b_0 = 0.15$ for the experiments of LW98. We also

note that $a_0/b_0 = 0.177$ corresponds to $r_c/b_0 = 0.2$, where r_c is defined as the radius from the centre of one vortex to where the tangential velocity is maximum ($r_c = 1.12a$ for a Lamb–Oseen vortex).

Superimposed on the base vortex flow, (2.4), is a three-dimensional random perturbation velocity field. The amplitude of the perturbations does not exceed $0.001W_{max}$ and is comparable to that used in previous simulations (Laporte & Corjon 2000). The corresponding vorticity perturbations are approximately 0.2 % of Ω_0. The initial temperature field corresponds to a uniform gradient ($\mathrm{d}\overline{T}/\mathrm{d}z > 0$) with no initial perturbations. We note that additional simulations were performed in which the velocity perturbation level was increased by a factor of 5. Results showed no significant change in growth rates of the linear instability. Use of different random fields, e.g. different random number generator seed, yielded variations in growth rate of up to 7 %.

The relevant non-dimensional parameters are now defined. The characteristic length scale is the initial vortex separation, b_0. The geometry is characterized by the dipole aspect ratio, a_0/b_0. The velocity scale is the initial advection velocity of the vortices, $W_0 = \Gamma_0/2\pi b_0$, where Γ_0 is the initial vortex circulation (figure 1). The convective time scale of the vortex flow is therefore $b_0/W_0 = 2\pi {b_0}^2/\Gamma_0$ which, as will be shown in § 3.3.3, is the time scale of the instability. The circulation Reynolds number is given by,

$$Re_\Gamma = \frac{\Gamma_0}{\nu} = \frac{2\pi b_0 W_0}{\nu}. \tag{2.5}$$

The Froude number is defined as,

$$Fr = \frac{W_0}{N b_0}, \tag{2.6}$$

where N is the buoyancy frequency,

$$N^2 = -\frac{g}{\rho_0}\frac{\mathrm{d}\overline{\rho}}{\mathrm{d}z} = \alpha_T g \frac{\mathrm{d}\overline{T}}{\mathrm{d}z}. \tag{2.7}$$

Thus, Fr can be considered as the ratio of the buoyancy time scale to the instability time scale. The Prandtl number is $Pr = \nu/\kappa$.

For all simulations performed, the Reynolds number of the vortex pair is $Re_\Gamma = 2400$. This is comparable to the experiments of LW98 in which Re_Γ ranges from 2400 to 2750. The Prandtl number is $Pr = 0.7$. The Froude numbers considered are $Fr = 1$, 2, 5 and 10 which cover a range of conditions corresponding to strong ($Fr = 1$), moderate ($Fr = 2$) and weak ($Fr = 5$, 10) stratification. In addition, $Fr = \infty$ corresponding to an unstratified flow is considered. Since the values of Re_Γ and a_0/b_0 are comparable to those of LW98 and also to the simulations of Laporte & Corjon (2000) who use $Re_\Gamma = 2400$ and $r_c/b_0 = 0.2$, the unstratified flow serves as a validation for the simulations in addition to providing a reference flow from which to study the effects of stratification.

As indicated earlier, our study is directed at the fundamental flow problem and not the practical application. We note that the simulated vortices do not adequately represent those in typical aircraft wakes which are characterized by much smaller aspect ratios, of order 0.01 (Delisi *et al.* 2003), and much higher Re_Γ. Simulations of tight core vortices would require very high resolution and/or appropriate subgrid-scale modelling (Holzäpfel 2004). However, it has been reported that LES results of high Re_Γ ($\sim 10^7$) show higher growth rates, but otherwise similar dynamics to the low Re_Γ

flows (Laporte & Leweke 2002). With regard to Fr, the range of values we consider is representative of stratification levels in the lower atmosphere (Switzer & Proctor 2000).

The numerical solution procedure is based on a second-order finite-difference scheme with second-order Adams–Bashforth time integration (Gerz, Schumann & Elghobashi 1989). The dimensions of the computational domain are $L_x = 6b_0$, $L_y = 6b_0$, $L_z = 18b_0$, with resolution of $192 \times 192 \times 576$ (uniform) grid points, respectively. This allows approximately 13 grid points across the core of each vortex. Preliminary studies of simulations with differing numbers of grid points showed a reasonably grids-independent solution for this resolution. In addition, energy spectra (see figure 15) show no energy accumulation at the highest wavenumbers further demonstrating adequate resolution.

Periodic boundary conditions are employed in all three directions. The transverse length, $L_x = 6b_0$, is sufficient to minimize the effects of neighbouring vortices through the linear instability phase in all flows. Based on linear internal wave theory (see § 3.2), we expect the generated waves to reach the boundary at the end of the linear phase only for the $Fr = 1$ case. Still further time would be required for the waves to interact with the neighbouring vortices and thus we do not expect significant interaction for the extent of the simulations, except perhaps in the late stages of the $Fr = 1$ flow (§ 3.4). Additional test simulations using $L_x = 12b_0$ showed no significant change in wavelength or growth rate (values of growth rate σ differed by less than 0.1 %). The vertical length, $L_z = 18b_0$, is extended to accommodate the downward descent of the vortices and associated wake, and to prevent the vortices and wake from encountering image vortices and their wakes.

The axial length, $L_y = 6b_0$, is selected to minimize the Crow instability. Using Crow's linear stability theory (neglecting the differences between Rankine and Oseen vortices), we have computed the most amplified wavelength for $r_c/b_0 = 0.2$ to be $7.4b_0$. However, this theory predicts that there will be non-zero growth rates for wavelengths greater than about $4.8b_0$. Since the axial length of our computational domain is $6b_0$, we have excluded the instability with maximum growth rate, but we might expect to see some slow growth of a Crow instability with a wavelength near the axial length of our computational domain. In our simulations, we observed some axial variations with a scale larger than predicted for the short-wave instability, but these variations showed none of the properties characteristic of the Crow instability. Results from simulations using different axial lengths indicate $L_y = 6b_0$ to be a good compromise in minimizing the development of the Crow instability while retaining a sufficient number of short-wave periods for evaluating statistics and spectra (see § 3.3.2). Additional simulations suggest that the observed axial and vortex-to-vortex variability in the instability amplitudes are due to sensitivity of the flow to the initial perturbation field. For the case of $Fr = 1$, some competition between neighbouring wave modes is exhibited (§ 3.3.2).

3. Results

In the results presented, the non-dimensional time is $t^* = tW_0/b_0$ and non-dimensional spatial coordinates are $X = x/b_0$, $Y = y/b_0$ and $Z = z/b_0$.

3.1. *Flow visualizations*

Figures 2–5 show the development of the three-dimensional vortex structures in the unstratified ($Fr = \infty$) and stratified ($Fr = 5, 2, 1$) flows. The structures are visualized by isosurfaces of the second invariant of the velocity gradient tensor, $II = (\boldsymbol{\omega}^2/2 - \boldsymbol{S}^2)/2$,

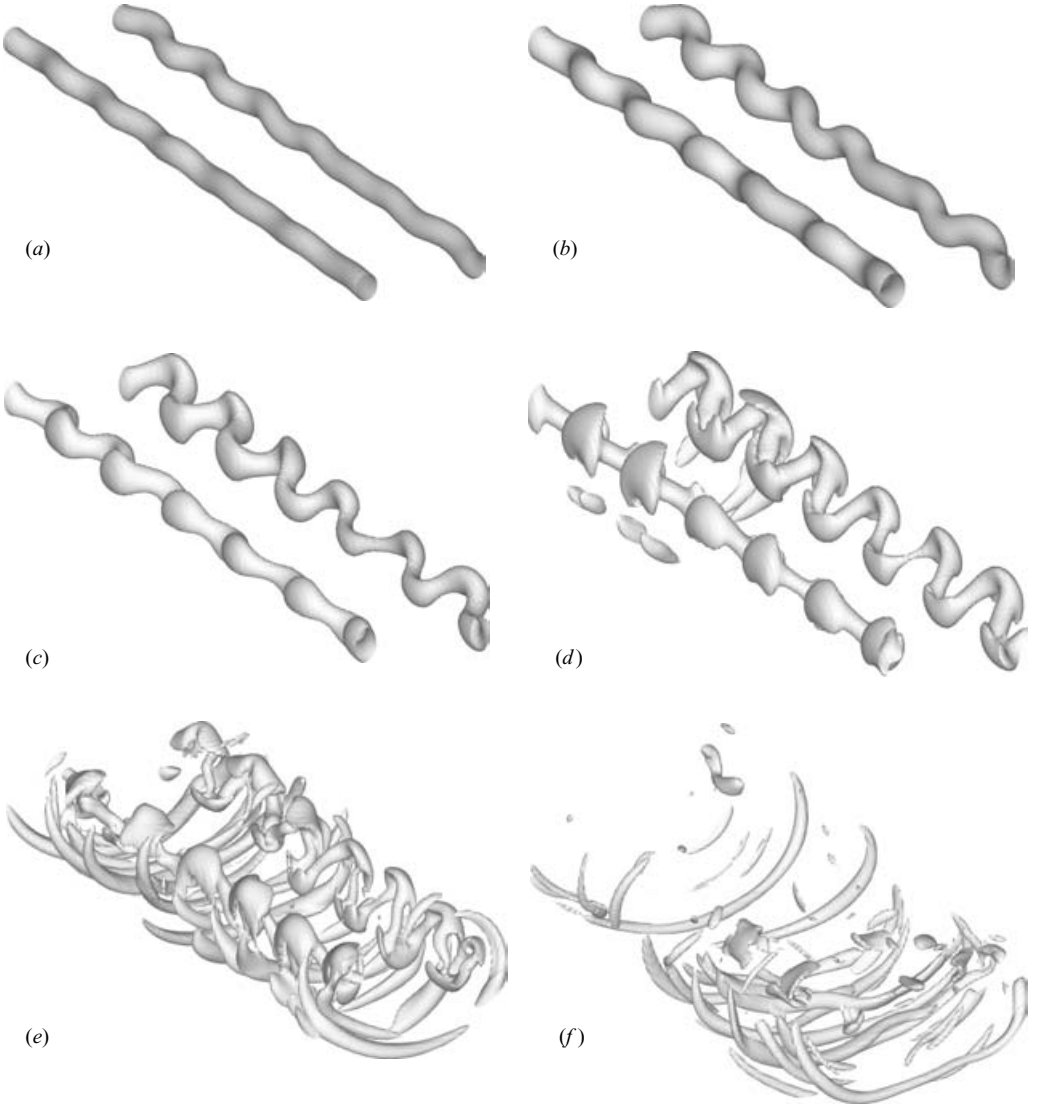

FIGURE 2. Three-dimensional visualizations of isosurfaces of the second invariant of velocity gradient tensor, II^* for $Fr=\infty$ at (*a*) $t^*=10.5$, (*b*) 12.0, (*c*) 13.5, (*d*) 15.0, (*e*) 16.5, (*f*) 18.0. (*a*) $II^*=40$, (*b–f*) 30.

where $\boldsymbol{\omega}$ is the vorticity vector and $\boldsymbol{S}$ is the strain rate tensor (Nomura & Post 1998). Here, it is non-dimensionalized as, $II^*=II/(\overline{\boldsymbol{\omega}_0^2}/4)$, where $\boldsymbol{\omega}_0$ is the initial vorticity. High-amplitude positive values of II thus correspond to strong rotation-dominated regions which effectively characterize the dominant vortex structures in the flow (Diamessis & Nomura 2000).

In the unstratified flow (figure 2), following an initial flow adjustment period (see § 3.2), the short-wave instability is initiated. A dominant wavelength is selected and amplified deforming the vortices in a sinusoidal manner that is antisymmetric with respect to the dividing plane between the vortices (figure 2*a*, *b*; $t^*\leqslant 12.0$). As the flow develops further, the geometry becomes more complex. Secondary structures develop

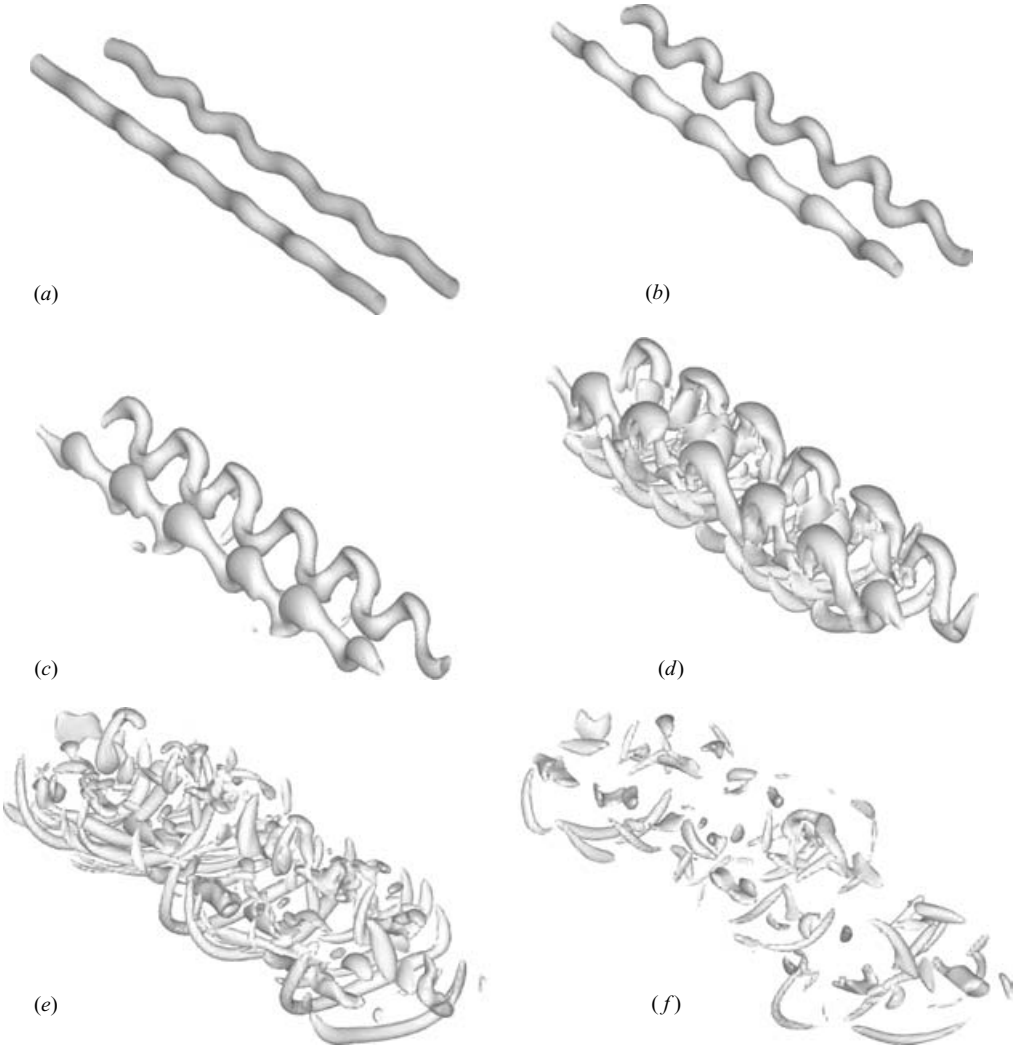

FIGURE 3. Three-dimensional visualizations of isosurfaces of the second invariant of velocity gradient tensor, II^* for $Fr = 5$ at (*a*) $t^* = 8.25$, (*b*) 9.0, (*c*) 9.75, (*d*) 10.5, (*e*) 11.25, (*f*) 12.0. (*a*) $II^* = 55$, (*b–e*) 50, (*f*) 45.

in the transverse direction (figure 2*d*, *e*; $t^* \geqslant 15.0$) and eventually dominate the flow as the primary vortices breakdown and weaken (figure 2*f*).

A similar instability is observed in the flows with weak ($Fr = 5$, figure 3*a*, *b*; $t^* \leqslant 9.0$) to moderate ($Fr = 2$, figure 4*a*, *b*; $t^* \leqslant 6.0$) stratification, with the onset occurring earlier with increasing stratification. A noticeable reduction in the vortex separation distance is also observed. As in the unstratified flow, the breakdown of the primary vortices is associated with the development of secondary vortex structures; however, these structures differ in the stratified flows. In the moderately stratified flow (figure 4*c*, *d*), vertical structures are formed. In weakly stratified flow (figure 3*d*, *e*), both vertical and transverse structures are observed. With strong stratification ($Fr = 1$, figure 5*a*, *b*, $t^* \leqslant 4.5$), the vortices are brought so close together that the core deformation becomes irregular. A smaller wavelength is indicated. Evidence of the

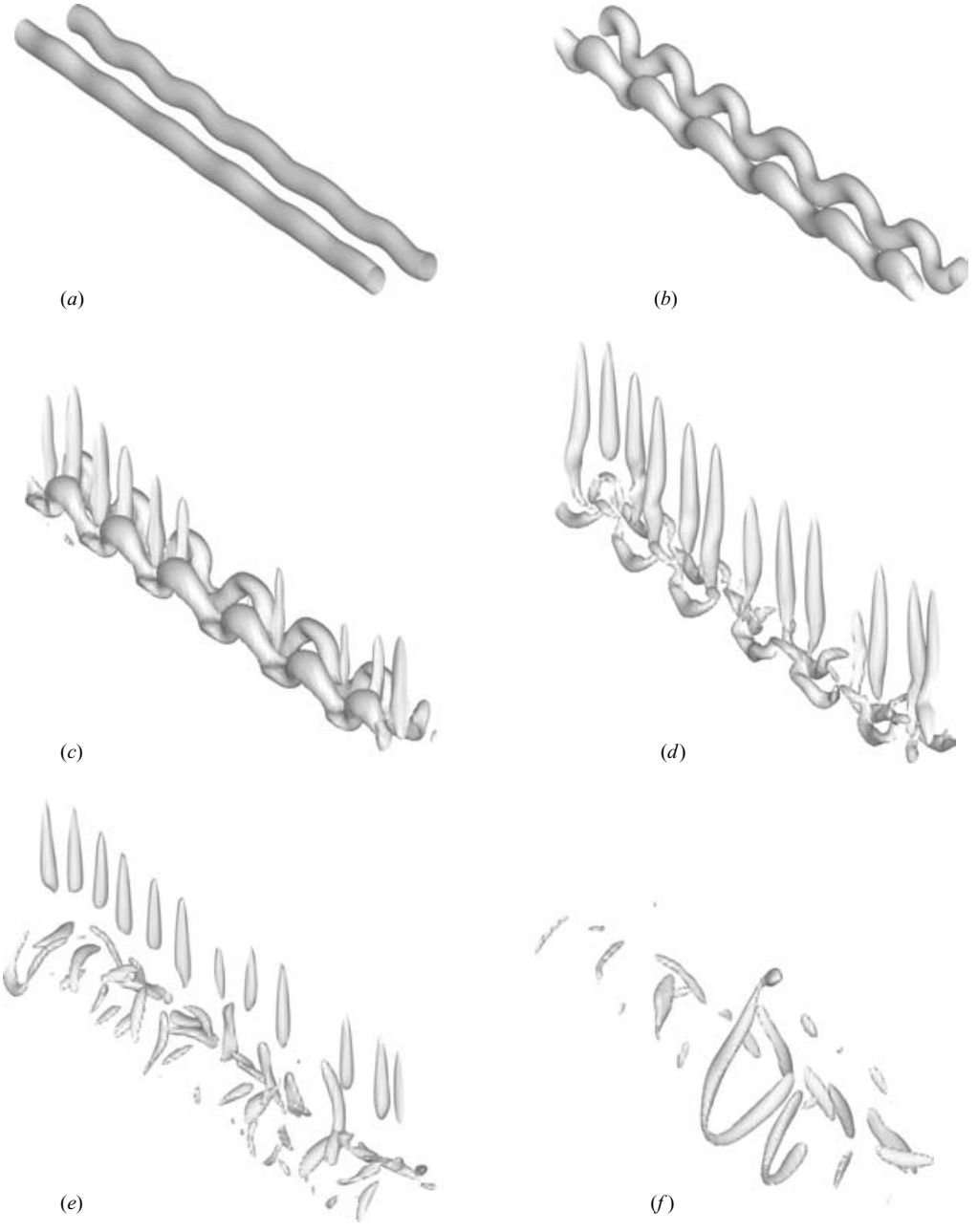

FIGURE 4. Three-dimensional visualizations of isosurfaces of the second invariant of velocity gradient tensor, II^* for $Fr = 2$ at (*a*) $t^* = 5.25$, (*b*) 6.0, (*c*) 6.75, (*d*) 7.5, (*e*) 8.25, (*f*) 9.0. (*a*) $II^* = 75$, (*a*) 60, (*c*) 45, (*d*) 40, (*e*, *f*) 25.

formation of vertical secondary structures between the primary vortices is observed (figure 5*c*, $t^* = 5.25$). More significant, however, is the appearance of structures in the wake of the primary vortices. As will be discussed, these structures are associated with baroclinically generated vorticity which in this flow is significant and eventually

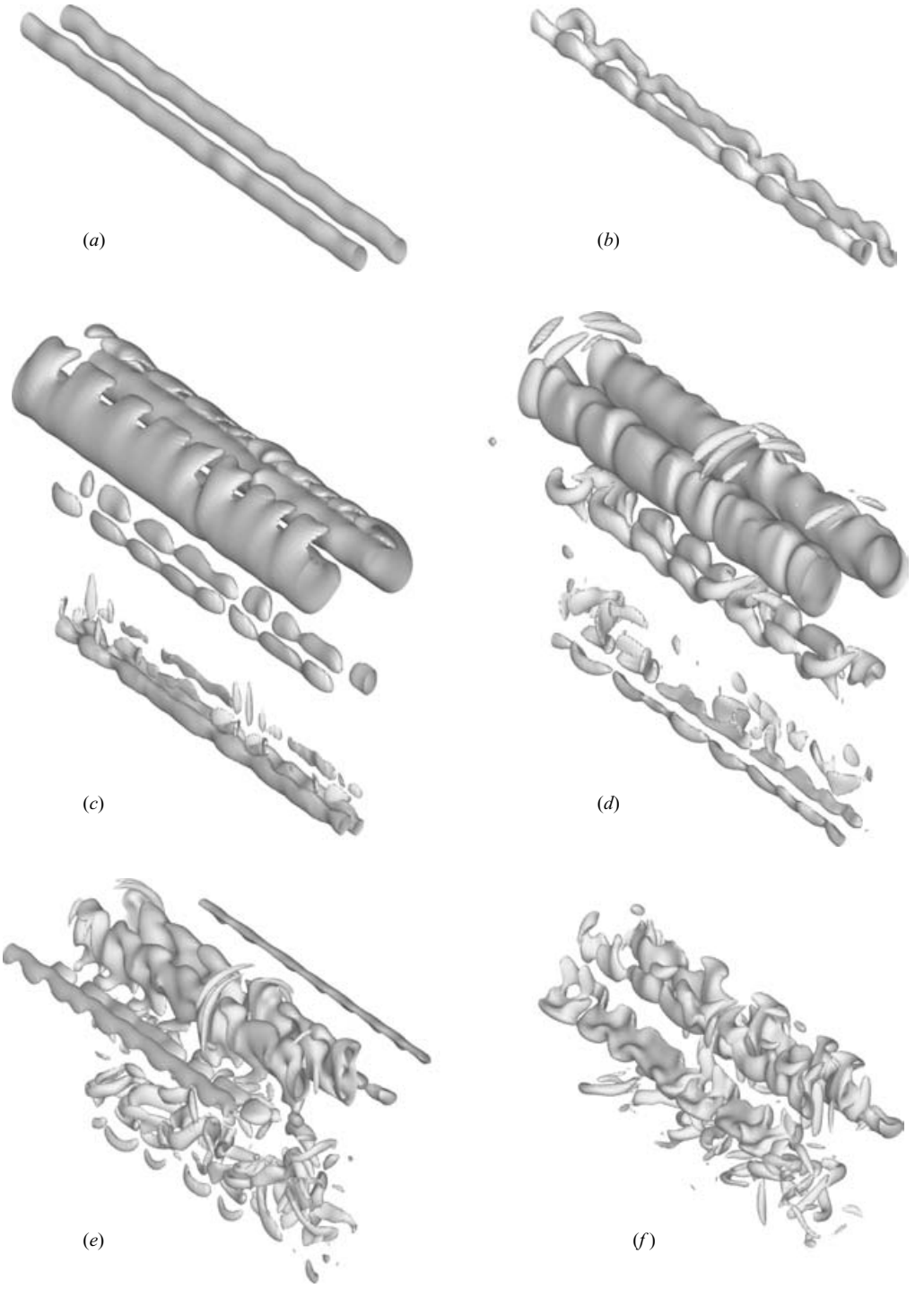

FIGURE 5. Three-dimensional visualizations of lower isosurfaces of the second invariant of velocity gradient tensor, II^* for $Fr = 1$ at (*a*) $t^* = 3.75$, (*b*) 4.5, (*c*) 5.25, (*d*) 6.0, (*e*) 6.75, (*f*) 7.5. (*a*) $II^* = 100$, (*b*) 70, (*c–f*) 7.

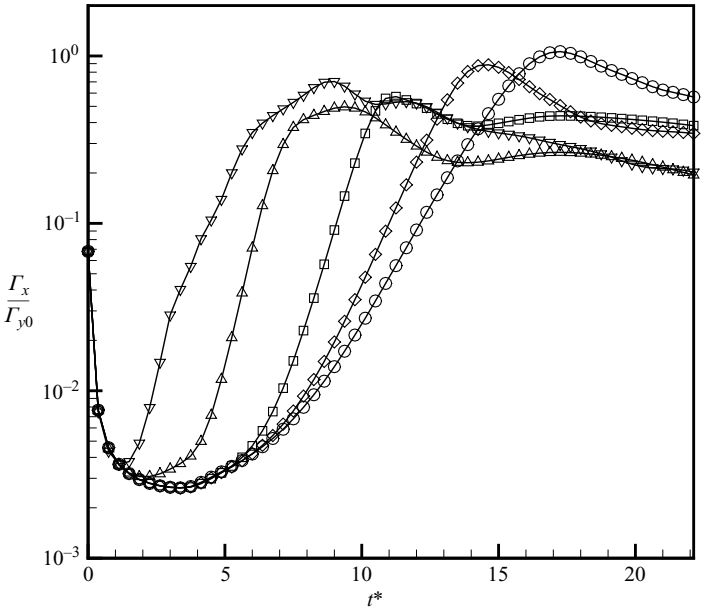

FIGURE 6. Time development of normalized average transverse vorticity magnitudes, $\Gamma_x/\Gamma_{y,0}$. Symbols: ○, $Fr=\infty$; ◇, 10; □, 5; △, 2; ▽, 1.

dominates the flow (figure 5*f*, $t^*=7.5$). Note the relatively low level of *II* associated with these regions, which is consistent with the sheet-like geometry of these structures.

Details of the observed flow structure and associated dynamics are presented in §§ 3.3 and 3.4. We first consider basic aspects of the overall evolution of the flow.

3.2. *General behaviour*

Since the initial flow is dominated by axial vorticity, ω_y, the development of the off-axial components of $\boldsymbol{\omega}$ provides an indicator of the instability and change from two-dimensional to three-dimensional flow. Following Laporte & Corjon (2000), a global measure of the transverse vorticity, ω_x, is given by,

$$\Gamma_x = \frac{1}{L_x}\int_{L_x}\left(\int_{L_y}\int_{L_z}|\omega_x(x,y,z)|\,\mathrm{d}y\,\mathrm{d}z\right)\mathrm{d}x. \tag{3.1}$$

Figure 6 shows the time development of Γ_x (normalized with the initial value of the axial vorticity magnitude $\Gamma_{y,0}$). Γ_x characterizes the evolution of the flow which can be considered to consist of three phases: *adjustment*, *linear* and *nonlinear* (Laporte & Corjon 2000). The adjustment phase ($0<t^*\lesssim 3.4$ for $Fr=\infty$) corresponds to the initial decrease in Γ_x. During this phase, the flow adjusts from its initial conditions as it develops under the Navier–Stokes equations. The vortices adapt to the presence of each other and owing to the induced velocity, they propagate downwards and develop an elliptic shape due to the mutually induced strain. The perturbation field decays owing to viscous diffusion and the flow remains two-dimensional. In the linear phase ($3.4\lesssim t^*\lesssim 13.5$ for $Fr=\infty$), Γ_x increases, although $\Gamma_x \ll \Gamma_y$. This phase corresponds to the development of the three-dimensional short-wave instability with growth of the perturbation amplitudes. The linear phase is limited to times in which the perturbation amplitudes remain small in comparison with the base flow and the core displacement exhibits an exponential growth as indicated by linear stability theory (see § 3.3.2).

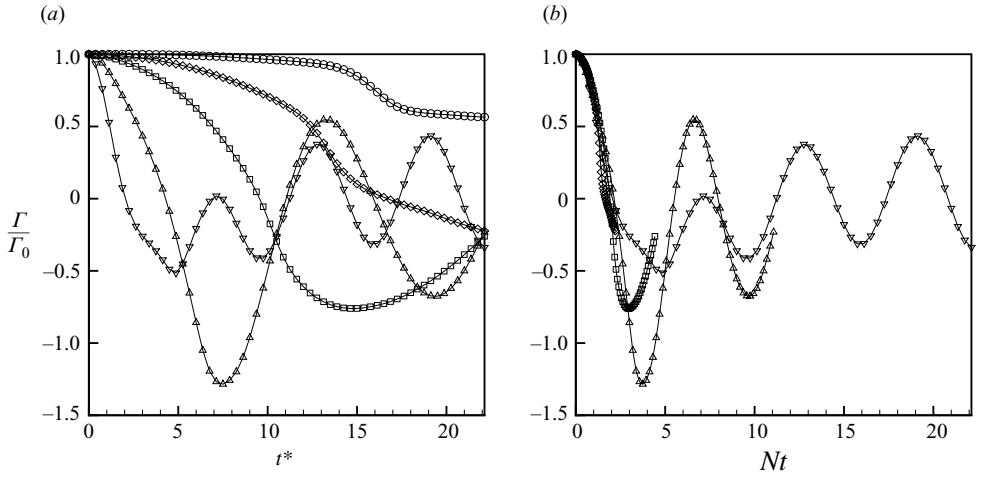

FIGURE 7. Time development of (*a*) vortex circulation, Γ, (*b*) vortex circulation with time rescaled with buoyancy scale $1/N$. ○, $Fr=\infty$; ◇, 10; □, 5; △, 2; ▽, 1.

When $\Gamma_x/\Gamma_{y,0}$ exceeds about 2 %, the deformation is clearly visible ($t^*=10.5$ for $Fr=\infty$, figure 2*a*) and three-dimensional dynamics become significant. For example, at the corresponding times, the orientation of the principal strains begins to change (see § 3.3.1 and figure 14*a*) indicating the significance of the modified vorticity. From figure 6, it is seen that the onset of the linear phase occurs earlier for the stratified flows and the growth rate of Γ_x increases with increasing stratification (decreasing Fr). In the nonlinear phase ($t^* \gtrsim 13.5$ for $Fr=\infty$), the perturbation amplitudes are significant and Γ_x becomes comparable in magnitude to Γ_y. Γ_x eventually reaches a peak and then decreases.

The vortex circulation, Γ (evaluated over half the transverse domain), is given by,

$$\Gamma = \frac{1}{L_y}\int_{L_x}\left(\int_{L_x/2}\int_{L_z}\omega_y(x,y,z)\,\mathrm{d}x\,\mathrm{d}z\right)\mathrm{d}y, \tag{3.2}$$

and shown in figure 7(*a*). In the unstratified flow ($Fr=\infty$), Γ corresponds to the circulation of one vortex and exhibits a moderate decrease in the linear phase ($t^* \lesssim 13.5$) and a more significant decrease in the nonlinear phase. In the stratified flows, Γ is seen to decrease more rapidly through both the linear and nonlinear phases. This is due primarily to the generation of baroclinic torque. As the vortex pair descends through the stably stratified fluid, it transports lighter fluid into a region of heavier fluid (figure 8*a*). Strong horizontal density gradients are thereby established which generate axial vorticity of opposite sign (figure 8*b*) through baroclinic torque, as described by the last term in the vorticity equation,

$$\frac{\partial\boldsymbol{\omega}}{\partial t} + (\boldsymbol{v}\cdot\nabla)\boldsymbol{\omega} = \boldsymbol{\omega}\cdot\nabla\boldsymbol{v} + \nu\nabla^2\boldsymbol{\omega} + \frac{1}{\rho_0}\nabla\rho\times\boldsymbol{g}. \tag{3.3}$$

Since this opposite signed vorticity is included in (3.2), Γ is reduced in value. The process is initially two-dimensional and begins immediately in the adjustment phase. However, once off-axial vorticity is established, axial components of the density gradient are generated which then establish transverse components of baroclinic torque. With moderate to strong stratification ($Fr \leqslant 2$ in figure 7*a*), Γ becomes negative and then oscillates in time. Figure 7(*b*), in which time is scaled by $1/N$, shows that this oscillation occurs at the buoyancy frequency (with period $2\pi/N$).

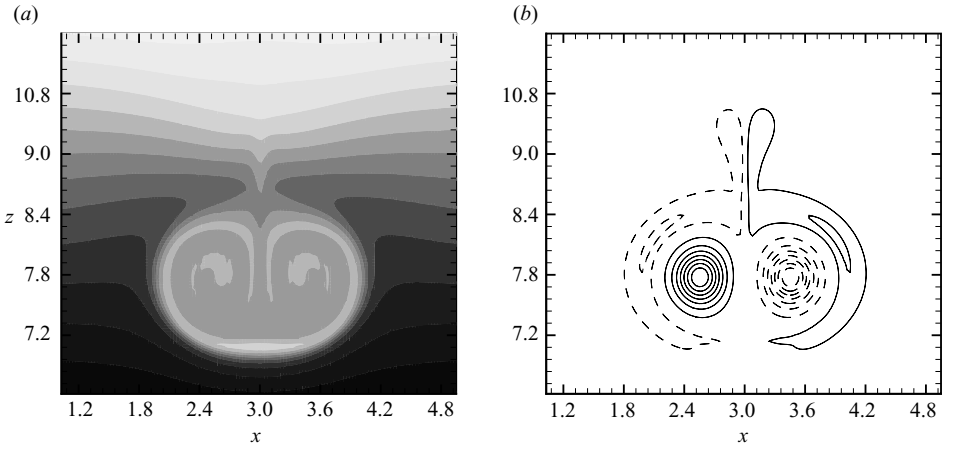

FIGURE 8. Contours in (x, y)-plane for $Fr = 2$ at $t^* = 2.25$ of (a) density, $\tilde{\rho}$ and (b) axial vorticity, ω_y (solid: $\omega_y > 0$, dashed: $\omega_y < 0$) showing generation of opposite signed vorticity by baroclinic torque (b) due to horizontal density gradients (a).

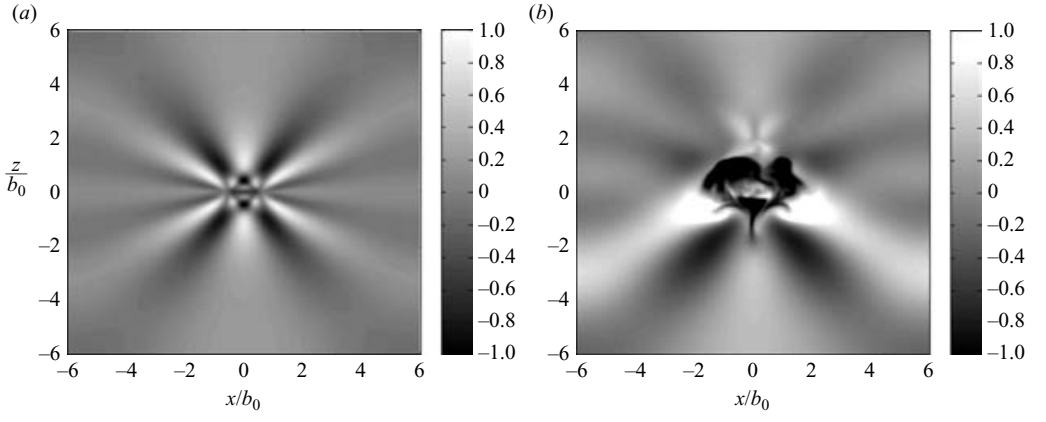

FIGURE 9. The non-dimensional temperature perturbation field showing internal wave generation and propagation from the vortex pair. The wave amplitudes have been normalized to have a maximum value of unity in each plot. (a) Linear analysis for $Nt = 10$, (b) simulation (extended domain) result for $Fr = 1$ at $Nt = 10$.

As discussed in Meng & Rottman (1988), a counter-rotating vortex pair generates an internal wave field that resembles an approximately two-dimensional fan of rays emanating from the region occupied by the vortex pair. This is illustrated in figure 9(a) which shows the perturbation temperature (T) field computed using linear theory (Meng & Rottman 1988). Figure 9(b) shows T in an (x, z)-plane from our nonlinear simulations for $Fr = 1$ at $t^* = Nt = 10$ $(t^* = FrNt)$. Although linear theory, in which the amplitudes of the waves are proportional to Fr, is strictly valid for $Fr \ll 1$, the two plots show similar qualitative features in the region away from the origin where the flow is dominated by the vortices.

We can use linear internal wave theory to estimate the time it takes for the internal waves generated by the vortex pair to reach the boundaries of the computational domain. As described in Meng & Rottman (1988), the radial position r with respect

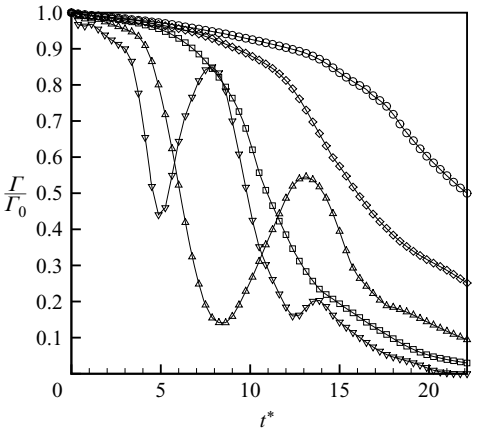

FIGURE 10. Time development of conditional vortex circulation, $\langle \Gamma \rangle_{\omega_{y+}}$ (conditioned by $\omega_y > 0$). ○, $Fr = \infty$; ◇, 10; □, 5; △, 2; ▽, 1.

to the origin and angular position θ with respect to the x-axis of the internal wave with wavenumber magnitude K and wavenumber angle ϕ is given by

$$\frac{r}{b_0} = \frac{Nt}{Kb_0}|\cos\theta|. \tag{3.4}$$

Since the wavenumber vector is perpendicular to the group velocity vector for internal waves, $\theta = \phi + \pi/2$. The dominant waves generated by the vortex pair have $Kb_0 \approx 1$, so the maximum radial distance travelled by these waves from the origin at time t is $r/b_0 \approx Nt$. Based on this estimate, we expect the dominant internal waves to reach the boundaries of the computational domain at $t^* = FrL_x/(2b_0)$. For $L_x = 6b_0$, this gives $t^* \approx 3$, 6, 15 and 30 for $Fr = 1$, 2, 5 and 10, respectively. Thus, as discussed in § 2, we do not expect significant contamination by waves entering through the periodic boundaries during the linear phase of these flows. There may, however, be some contamination during the nonlinear phase of the strongly stratified ($Fr \sim 1$) flows.

Figure 10 shows a conditional vortex circulation $\langle \Gamma \rangle_{\omega_{y+}}$ (conditioned on $\omega_y > 0$) which effectively excludes the baroclinic vorticity and provides a measure of the circulation of the primary vortex, at early times in the flow. A more moderate reduction during the linear phase followed by an enhanced decay during the nonlinear phase is revealed. The rate of decay increases with increasing stratification. At late times, this simple conditional averaging is no longer meaningful owing to the complexity of the flow. As discussed in § 3.4, during the late stages of strongly stratified flows, there is successive generation of opposite signed baroclinic torque (for $Fr = 1$, this occurs for $t^* > 5$). Secondary baroclinic torque will have the same sign as the primary vortices and therefore be retained in $\langle \Gamma \rangle_{\omega_{y+}}$, thus rendering the conditional averaging ineffective.

Figure 11 shows the time development of the vortex pair descent height, H. Since H is defined with respect to the core centre (vorticity maximum), it can be evaluated only during the linear phase when the primary vortices are identifiable. During the early stages of development, the unstratified and weakly stratified flows exhibit a nearly constant descent speed. In the moderate to strongly stratified flows, the influence of stratification is observed. In the $Fr = 1$ flow, the descent is arrested for a period of time before it resumes. In general, the duration of the linear phase decreases with

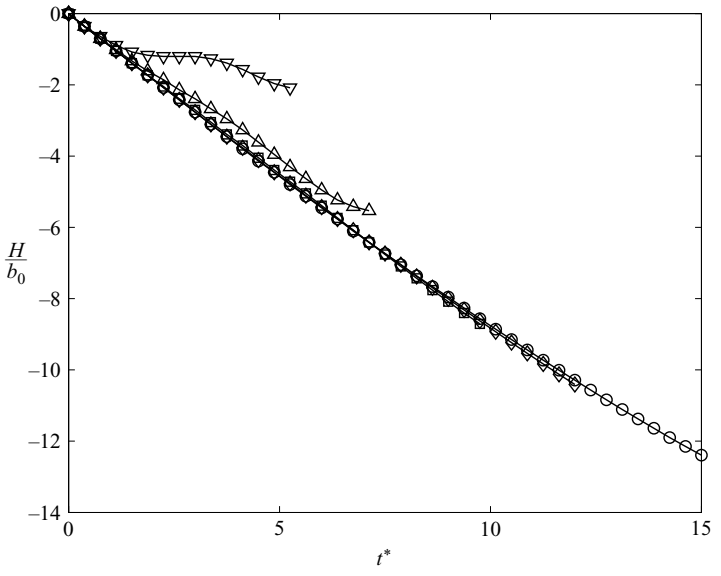

FIGURE 11. Vortex pair descent height, H, normalized by b_0. ○, $Fr = \infty$; ◇, 10; □, 5; △, 2; ▽, 1.

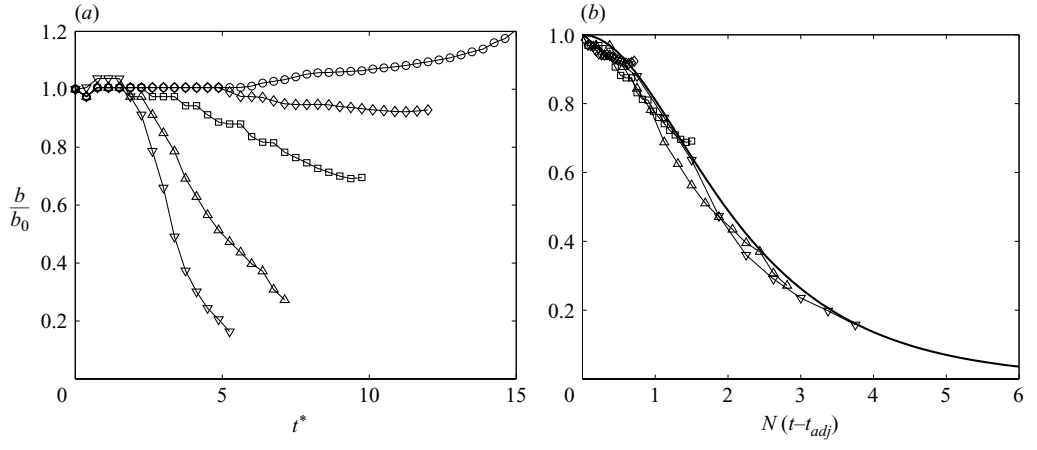

FIGURE 12. Time development of (a) vortex separation, b, normalized by b_0, (b) vortex separation with time rescaled with the buoyancy time scale $1/N$. ○, $Fr = \infty$; ◇, 10; □, 5; △, 2; ▽, 1. Here, t_{adj} is the adjustment time beyond which b starts to decrease in (a). Solid line in (b) corresponds to the theory given by equation (3.5).

increasing stratification. The behaviour of H is consistent with previous results of Holzäpfel *et al.* (2001).

Figure 12(a) shows the time development of the vortex separation distance, b. In the stratified flows, b decreases in time; the rate of decrease increasing with increasing stratification. As discussed earlier, the reduction of b is due to the secondary flow associated with the generated baroclinic torque which advects the primary vortices towards one another. The behaviour is described by the analyses of Saffman (1972) and Crow (1974), which are reviewed in Spalart (1996). Their analysis considers a two-dimensional quasi-steady nearly inviscid flow with weak stratification and gives

the following result for $b(t)$:

$$b(t) = \frac{b_0}{\cosh\left((A/2\pi)^{1/2} Nt\right)}, \tag{3.5}$$

where $A = 2.85$ (Saffman 1972). This solution is shown in figure 12(b) along with the simulation results which are scaled by $N(t - t_{adj})$. Here, t_{adj} is the adjustment time beyond which b starts to decrease (figure 12a) and b is rescaled with the separation distance at the corresponding time. As figure 12(b) shows, the simulation results are in reasonable agreement with the theory, indicating that the behaviour of $b(t)$ is primarily controlled by two-dimensional dynamics.

We note that in strongly stratified flow ($Fr \sim 1$), the effects of baroclinic torque significantly alter the flow early in time, i.e. during the linear phase. The reduction in separation distance b is so significant that the primary vortices are brought together (see figure 26b, $t^* \leqslant 4.5$). Mutual diffusion of opposite sign vorticity reduces their strength (as observed in figure 10) and size. In addition, as also indicated in figure 26(b), baroclinic torque causes detrainment of the primary vortices further reducing their size.

Details of the linear and nonlinear phases are presented in the following sections.

3.3. *Linear phase*

3.3.1. *Geometric features of short-wave instability*

As discussed in LW98, the three-dimensional short-wave instability is an elliptic instability which evolves in the vortex pair in a coupled 'cooperative' manner. Close examination of the vortices reveals the distinct geometry associated with this instability which is also exhibited in the weak to moderately stratified flows.

As seen in the unstratified flow (figure 13a–c), the deformation of the core is in phase when viewed from the bottom (x, y-plane, figure 13a) and out-of-phase when viewed from the side (y, z-plane, figure 13b); the core displacements are of an anti-symmetric mode. As discussed earlier, some axial variation is present owing to the random initial perturbations. In the bottom view (figure 13a), both the inner core (high vorticity magnitude) and outer layer (low vorticity magnitude) are displayed. We see that the inner and outer regions of the vortex are displaced in opposite directions. Note that in these visualizations, vorticity magnitude is used rather than II in order to distinguish the outer layer better. These geometric features are consistent with the experimental observations of LW98. In the (x, z)-plane (end view, figure 13c), the deformation of each vortex (at this time) is seen to orient in a plane approximately $20^\circ - 22^\circ$ from the horizontal. This angle of the deformation plane from the horizontal (as viewed in the (x, z) plane) will be referred to as θ_ω. In the stratified flow ($Fr = 2$, figure 13d–f), the basic geometric features of the elliptic instability are retained although, notably, the vortex separation is reduced (figure 13d) and the angle of the deformation plane is larger ($\theta_\omega \approx 47^\circ - 50^\circ$, figure 13$f$).

The orientation of the deformation plane is presumed to correspond to the direction of the principal extensional strain (LW98). From the simulation results, the principal eigenvalues of the rate of strain tensor were determined at the core centre, in particular, the most extensional strain, α, and the corresponding eigenvector $\boldsymbol{e}_\alpha$. Figure 14(a) shows the time development of θ_α, defined as the angle from the horizontal of $\boldsymbol{e}_\alpha$ as projected onto the (x, z)-plane (axial average). For weak (and zero) stratification ($Fr \geqslant 5$), θ_α remains at nearly 45° during the linear phase and then increases as the flow becomes three-dimensional and the nonlinear phase begins. With strong stratification

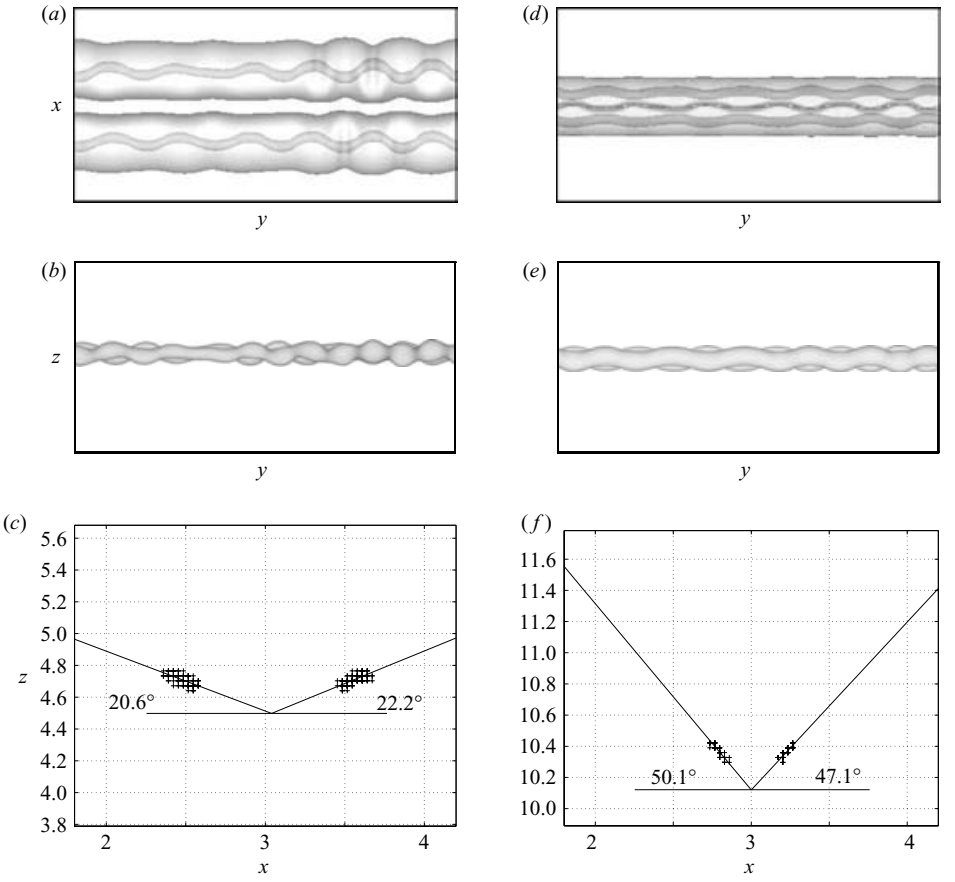

FIGURE 13. Geometry of elliptic instability for (*a*)–(*c*) $Fr = \infty$ ($t^* = 12.0$) and (*d*)–(*f*) $Fr = 2$ ($t^* = 5.625$). (*a*), (*c*) Bottom views of two isosurfaces of high and low vorticity magnitude (normalized with initial maximum value, $|\omega_0|_{max}$) indicating inner core and outer layer, respectively, (*a*) $|\omega|_{high}/|\omega_0|_{max} = 0.19$, $|\omega|_{low}/|\omega_0|_{max} = 0.025$, (*c*) $|\omega|_{high}/|\omega_0|_{max} = 0.30$, $|\omega|_{low}/|\omega_0|_{max} = 0.030$. (*b*), (*e*) Side views of isosurface of high vorticity magnitude. (*c*), (*f*) End views showing vortex centre (maximum vorticity) locations projected onto the (x, z)-plane. The angles of the deformation plane, θ_ω, with respect to horizontal are indicated for each vortex.

($Fr = 1$), θ_α exhibits an increase during the linear phase. Figure 14(*b*) shows the time development of θ_α together with the angle of the core deformation, θ_ω. As indicated in the figure, early in time, θ_ω is smaller than θ_α. This is consistent with the expected behaviour of the vorticity. Initially, the axial (horizontal) component ω_y dominates. As vorticity perturbations in the direction of largest positive strain ($\boldsymbol{e}_\alpha$) amplify, the angle of the vorticity vector from the horizontal increases. When the perturbation vorticity becomes significant, the core deformation is observable and θ_ω approaches 45° for $Fr \geqslant 5$. At the same time, the induced strain by the deformed core becomes significant and θ_α deviates from 45° (and (x, z)-plane as $\boldsymbol{e}_\alpha$ indicates, not shown). Thus, as indicated in figure 14(*b*), the deformation is not aligned with $\boldsymbol{e}_\alpha$ in these cases. Three-dimensional effects are signficant and the interaction of $\boldsymbol{\omega}$ and $\boldsymbol{S}$ must be considered (Nomura & Post 1998). With stratification, θ_ω increases more rapidly and achieves a higher value. As will be shown, there is an enhancement of strain in these flows which accelerates the growth of the vorticity perturbations. With strong

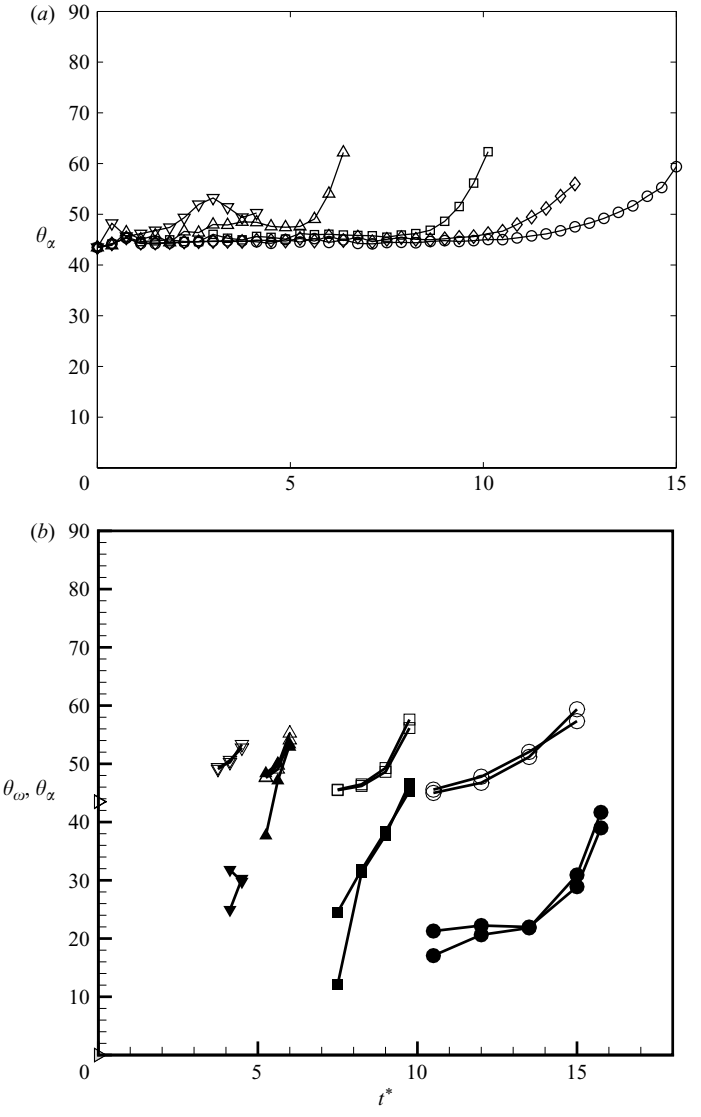

FIGURE 14. Time development of (*a*) angle of eigenvector of the most extensional principal strain, θ_α, and (*b*) angle of vortex core deformation, θ_ω, along with corresponding θ_α. Both angles are measured from the horizontal in the (x, y)-plane. Open symbols for θ_α, solid symbols for θ_ω: ○, $Fr = \infty$; ◇, 10; □, 5; △, 2; ▽, 1.

stratifcation ($Fr = 1$), the linear phase is short-lived and the deformation does not develop to a sufficient extent for θ_ω to develop significantly before the cores become indiscernible.

3.3.2. *Wavelength and growth rate*

In order to carry out a quantitative assessment of the linear phase, the axial wavelength of the instability, λ, and the corresponding growth rate, σ, are determined. The spectral energy $E_k(t)$ is obtained by performing a one-dimensional Fourier transform in the axial (y) direction of each velocity component which yields, $\hat{\boldsymbol{v}} = \hat{\boldsymbol{v}}(x, k, z, t)$,

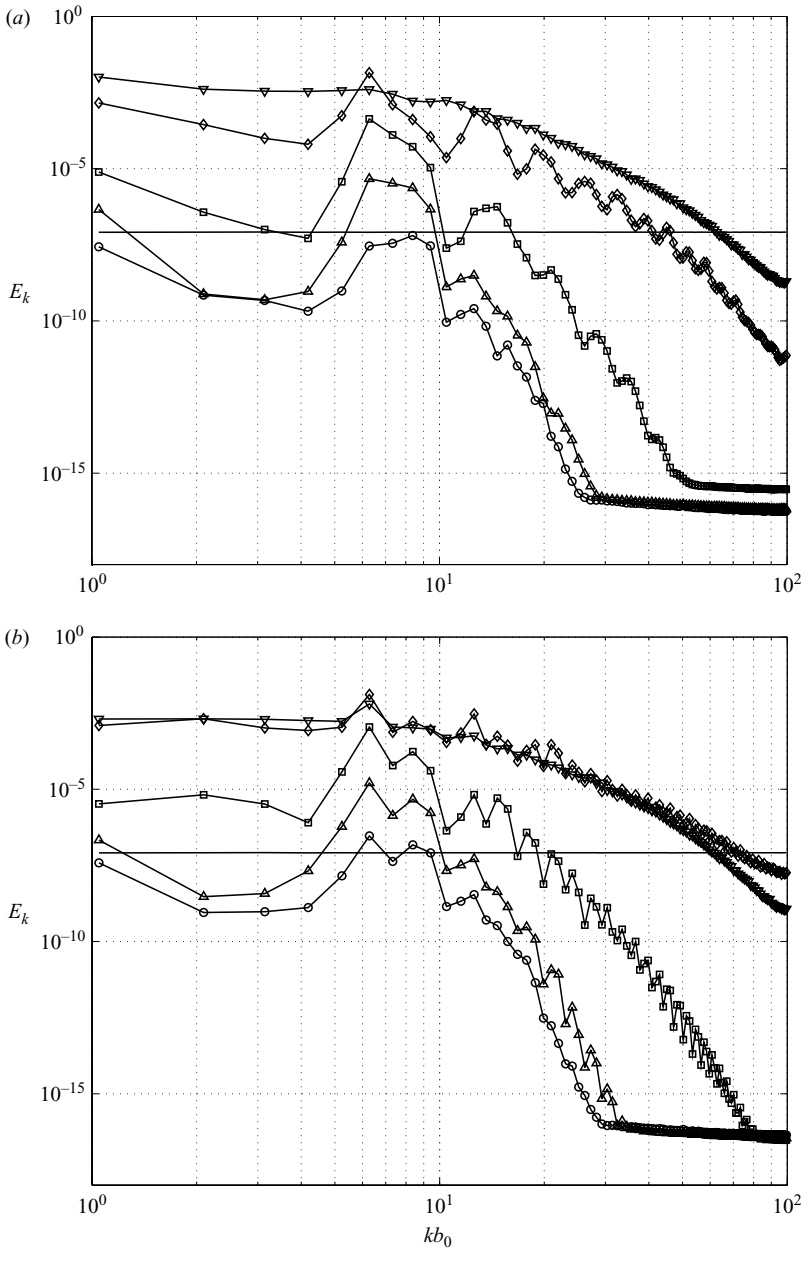

FIGURE 15(*a–d*). For caption see facing page.

and then evaluating the average of $\widehat{\boldsymbol{v}} \cdot \widehat{\boldsymbol{v}}^*$ in the transverse (x, z)-plane,

$$E_k(t) = \frac{1}{L_x L_z} \int_x \int_z \widehat{\boldsymbol{v}} \cdot \widehat{\boldsymbol{v}}^* \, \mathrm{d}x \, \mathrm{d}z, \tag{3.6}$$

where $\widehat{\boldsymbol{v}}^*$ denotes the complex conjugate. Since the base flow is two-dimensional in the (x, z)-plane, $E_k(t)$ for $k > 0$ corresponds to the perturbation kinetic energy. The wavenumber, $k = 2\pi/\lambda$, is non-dimensionalized by b_0 and related to the Fourier mode

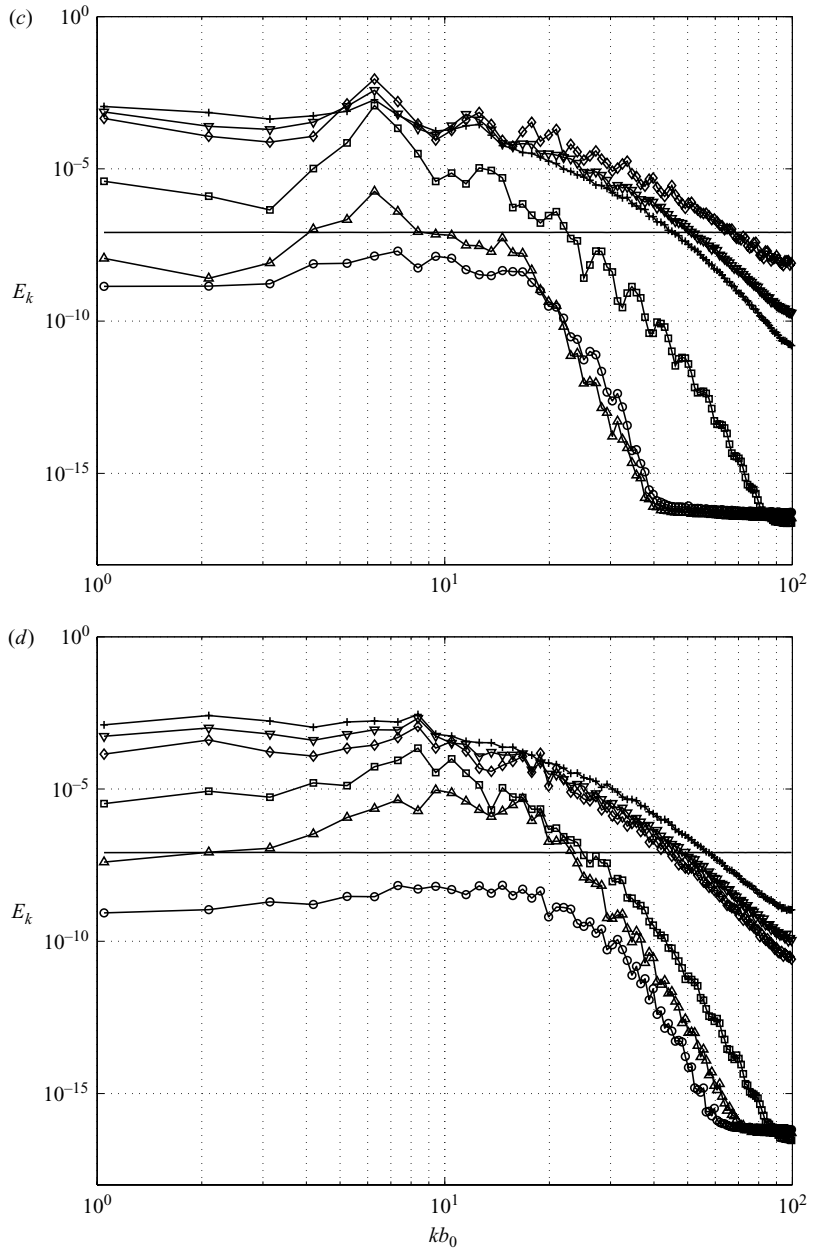

FIGURE 15. Kinetic energy spectrum for (*a*) $Fr = \infty$: $t^* = 0, 6, 9, 12, 15, 18$, (*b*) $Fr = 5$: $t^* = 0, 6, 7.5, 9, 10.5, 12$, (*c*) $Fr = 2$: $t^* = 0, 3, 4.5, 6, 7.5, 9, 10.5$, (*d*) $Fr = 1$: $t^* = 0, 1.5, 3, 4.5, 6, 7.5, 9$. Symobols: ○, △, □, ◇, ▽, and + correspond to each time, $t > 0$, in ascending order. Solid line correponds to $t^* = 0$.

number, $m = L_y/\lambda = 6b_0/\lambda$, by,

$$kb_0 = \frac{2\pi b_0}{\lambda} = \frac{m\pi}{3}. \tag{3.7}$$

Figure 15(*a*) shows spectra $E_k(t)$ for the unstratified flow. Initially ($t^* = 0$), the spectrum is flat corresponding to the random perturbation field. During the adjustment

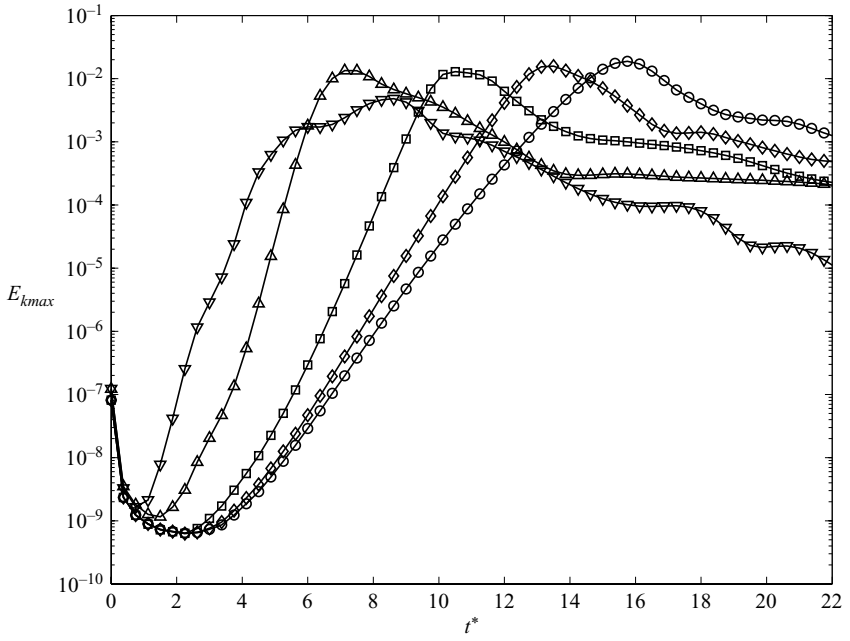

FIGURE 16. Evolution of perturbation energy of most amplified mode, $k = k_{max}$ (where k_{max} corresponds to the dominant peak in $E_k(t)$ in figure 15). ○, $Fr = \infty$; ◇, 10; □, 5; △, 2; ▽, 1.

phase (not shown), all axial wave modes decay owing to viscous diffusion, and energy at the high wavenumbers decays more quickly. Beyond the adjustment phase, the perturbation energy increases at the low wavenumbers. A dominant wavenumber, $k_{max}b_0 = 6\pi/3 = 6.3$, is identified (figure 15*a*, $t^* \geqslant 9$) indicating that the most amplified wavelength is $\lambda/b_0 = 1.0$. This compares reasonably well with the reported wavelength of $\lambda/b_0 = 0.77$ ($k_{max}b_0 = 8.16$) in the experiments of LW98 and $\lambda/b_0 = 0.85 \pm 0.05$ in the simulations of Laporte & Corjon (2000). We note that some discrepancy will arise from the finite computational domain of the simulations which requires approximating the Fourier transform with a discrete Fourier transform which allows only discrete wavenumbers. This limits the possible values of wavelength to $\lambda/b_0 = 6/m, m = 1, 2, \ldots, N_y/2$, where N_y is the number of grid points in the axial direction. For $m = 6$, the actual wavelength could have a value in the range of $0.86 < \lambda/b_0 < 1.2$. As discussed earlier, L_y is limited in order to minimize the effects of the Crow instability. Although varying L_y slightly might yield a better estimate of λ, there are other factors to be considered in assessing the results (see § 3.3.3).

Figure 16 shows the time development of $E_{k_{max}}(t)$. The growth rate, σ, of the most amplified mode energy is obtained from $\sigma = 1/2(\mathrm{d} \ln E_{k_{max}}/\mathrm{d}t)$. For $Fr = \infty$, the non-dimensional growth rate is $\sigma^* = \sigma/(\Gamma/2\pi {b_0}^2) = 0.83$. This is in agreement with the growth rates reported in LW98 ($\sigma^* = 0.94 \pm 0.12$) and in Laporte & Corjon (2000) ($\sigma^* = 0.96 \pm 0.3$).

In the stratified flows (figure 15*b–d*), $E_k(t)$ develops in a qualitatively similar manner to the unstratified flow during the adjustment and linear phases. In weak to moderate stratification ($Fr = 5, 2$, figure 15*b*, *c*) the same dominant wavenumber, $k_{max}b_0 = 6.3$, is exhibited. In strong stratification ($Fr = 1$, figure 15*d*), the peak occurs at a higher wavenumber, $k_{max}b_0 = 8\pi/3 = 8.4$. In general, the behaviour of $E_{k_{max}}(t)$ in figure 16 suggests that the growth rate increases with increasing stratification. However, in

Fr		∞	10	5	2	1
λ/b_0		1.0	1.0	1.0	1.0	0.75
$\sigma^* = \sigma/(\Gamma/2\pi {b_0}^2)$	Right vortex	0.74	0.89	1.26	1.60	2.09
	Left vortex	0.70	0.89	1.42	1.99	1.62
$\sigma_b^* = \sigma/(W_0/b)$	(Right vortex)	0.80	0.82	0.88	0.64	0.73
	(Left vortex)	0.76	0.82	0.99	0.80	0.57

TABLE 1. Computed wavelength and growth rates.

the stratified flows, the perturbation energy also includes that associated with the secondary flow due to the baroclinic torque. Thus for these flows, λ/b_0 and σ^* are determined using an alternative method based on the measured growth of the vortex core displacement (Mahoney 2002; Tsutsui 2003). A one-dimensional discrete Fourier transform is applied in the axial direction to the measured core displacements. The growth rate is determined by an exponential fit to the time development of the amplitude of the most amplified mode. It should be noted that the exponential function fits the simulation data well, indicating the existence and extent of the linear phase. Results are presented in table 1. As discussed earlier, there is some vortex-to-vortex variability in the instability amplitudes owing to sensitivity of the flow to the initial perturbation field. Note that the average growth rate for $Fr = \infty$ is $\sigma^* = 0.72$ which is in reasonable agreement with that obtained from $E_k(t)$. For weak to moderate stratification ($\infty > Fr \geqslant 2$), $\lambda/b_0 = 1.0$ as in the unstratified flow. However, as the stratification increases, σ^* increases. As will be discussed in § 3.3.3, this is due to the enhanced strain in the vortices resulting from the reduced vortex separation distance.

In the case of strong stratification ($Fr = 1$), both $E_k(t)$ (figure 15*d*) and the core displacement spectrum indicate that the most amplified wave mode is associated with a higher wavenumber, $k_{max} b_0 = 8\pi/3 = 8.4$ which corresponds to a shorter wavelength, $\lambda/b_0 = 0.75$. Results from additional simulations (different initial conditions, domain size) indicate comparable growth rates for wave modes in the range $6\pi/3 \leqslant k_{max} b_0 \leqslant 10\pi/3$.

To further assess the nature of the $Fr = 1$ flow, we consider details of the structure of the perturbation field. In particular, we consider the radial structure which can be understood by using results from Waleffe (1990) who analysed the elliptic instability in an unbounded single vortex. In this case, the axial perturbation velocity, v, is given by (in cylindrical coordinates with respect to the vortex),

$$v(r, \phi, y) = C \exp(\sigma t) J_1(\sqrt{3}\, k\, r) \sin(k\, y) \sin\left(\phi + \tfrac{1}{4}\pi\right) \tag{3.8}$$

where C is a constant and J_1 is the Bessel function of the first kind. The radial dependence of v, which is the same as that of the axial perturbation vorticity, is given by $J_1(\sqrt{3}kr)$. Figure 17(*a*) shows the distribution given by (3.8). If the vortex core contains only the inner dipole, this corresponds to the first radial mode. If the vortex core contains the inner dipole and its neighbouring pair, this corresponds to the second radial mode, and so on. As discussed by Billant *et al.* (1999), the Lamb–Chaplygin vortex pair (bounded and distributed vorticity) exhibits a similar internal structure (see their figure 4).

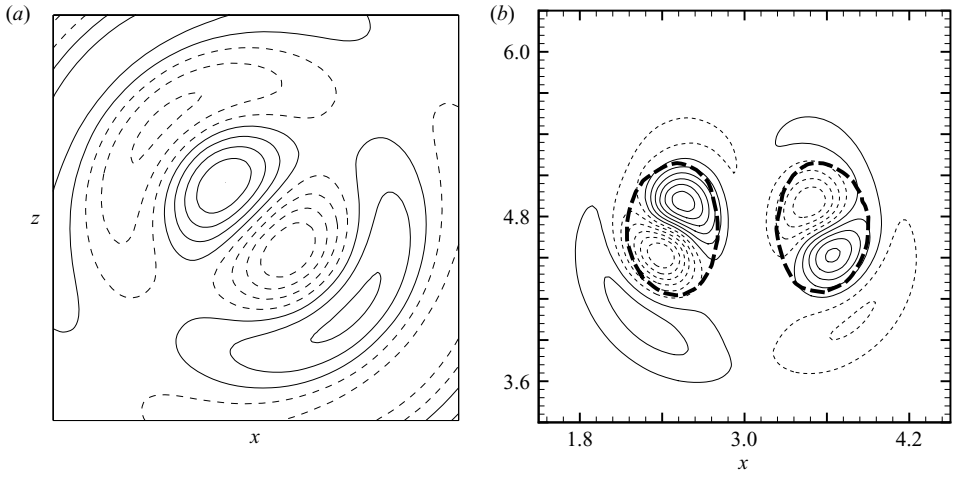

FIGURE 17. Axial component of perturbation velocity (a) theoretical prediction for single vortex (Waleffe 1990). The innermost pair corresponds to the first radial mode, the two innermost pairs correspond to the second radial mode, and so on. (b) DNS results for $Fr = \infty$, $t^* = 12.0$. The distribution indicates the first radial mode. Dashed-line shows axial vorticity contour corresponding to $|\omega|/|\omega|_{max} = 1/e$.

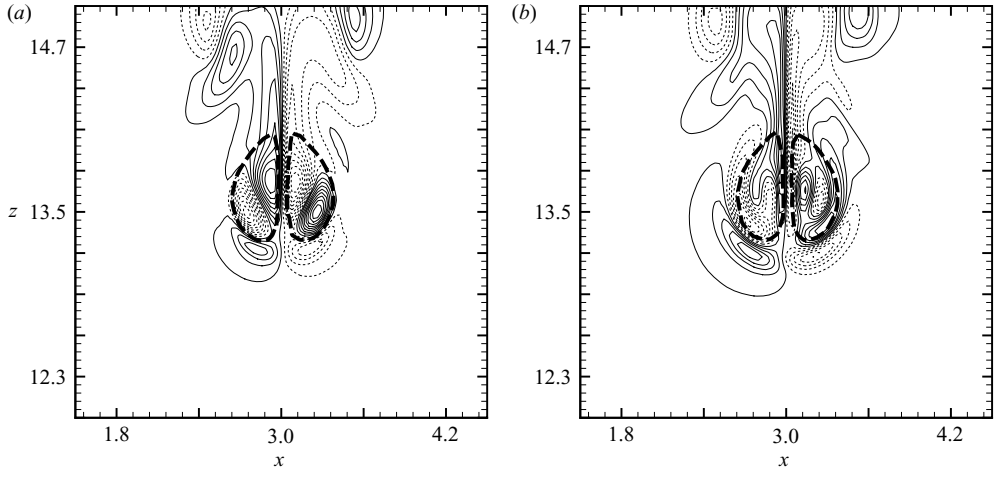

FIGURE 18. Axial component of perturbation velocity for $Fr = 1$, $t^* = 3.75$. (a) Distribution at axial location $y = 0.03b_0$ indicating the first radial mode. (b) Distribution at axial location $y = 0.11b_0$ indicating the second radial mode. Dashed-line shows axial vorticity contour corresponding to $|\omega|/|\omega|_{max} = 1/e$.

Figure 17(b) shows the distribution of axial perturbation velocity in a transverse plane in the unstratified flow ($Fr = \infty$). The region enclosed by the heavy dashed lines is the approximate spatial extent of the primary vortex cores. The figure indicates the first radial mode which is observed along the entire axial length of the vortices. The same behaviour is found in the weak to moderately stratified flows. In the strongly stratified flow ($Fr = 1$, figure 18), both the first and second radial modes are exhibited at different axial locations on the same vortex. As indicated in the figures, the shape of the primary vortices is not elliptical. The vortices are pushed against each other

and deform into a flattened tear-drop shape. As previously indicated, the combined action of mutual diffusion and detrainment reduces the size of the vortices.

3.3.3. *Discussion*

In order to understand and interpret the simulation results better, we review the existing theory for the short-wavelength instability in the unstratified vortex pair. As indicated in § 1, there are no stability analysis results for the stratified flow; thus, a reasonable approach is to consider first relatively weak stratification and how it will affect the known instability in unstratified flow. We will first consider the results of inviscid linear stability analysis. In this case, the fundamental parameter is the dipole aspect ratio, a/b, and both the vortex radius, a, and the vortex separation, b, are constant in the two-dimensional base flow. We will then consider results from a linear stability analysis in which viscous effects, characterized by Re_Γ, are considered. As discussed in Sipp & Jacquin (2003), viscosity will not only affect the perturbation growth rate, but also the base flow vortex radii, a. We will then discuss the present results for a vortex pair in a stably stratified fluid, in which the base flow also changes in time. Stratification is characterized by Fr which indicates the time scale of stratification to that of the flow instability. As our results indicate, two-dimensional effects of stratification may cause both a and b to vary in time. In the case of weak to moderate stratification, characteristics of the observed instability are fundamentally similar to that in unstratified flow. However, for strong stratification ($Fr \sim 1$), significant differences are observed and the existing theory for unstratified flow may no longer be applicable.

A number of theoretical studies have been carried out on the short-wave elliptic instability of a single vortex (e.g. Tsai & Widnall 1976; Waleffe 1990; Eloy & Le Dizès 1999). These studies showed that the axial wavenumber scales with a and the growth rate with strain rate. As the wavenumber increases, the radial structure becomes more complex. More relevant to the present work are the linear stability analyses performed for a vortex pair (Billant *et al.* 1999; Sipp & Jacquin 2003), which directly consider the parameter a/b. The inviscid analysis of Sipp & Jacquin (2003) considered the Lamb–Oseen vortex pair with two values of the dipole aspect ratio, $a/b = 0.208$ and 0.288. They found that the antisymmetric instability mode occupies bands of wavenumbers with a local maximum growth rate in each band. The wavenumbers corresponding to the maximum growth rate in the first three bands are: $ka = 2.26$, 3.96 and 5.61, corresponding to the first, second and third radial modes, respectively. For $a/b = 0.288$, the maximum growth rate of the first radial mode is higher than that of the second radial mode. Similar results were found by Billant *et al.* (1999) in a linear stability analysis of a Lamb–Chaplygin vortex pair with $a/b = 0.4478$. These results indicate that for sufficiently high a/b, the antisymmetric mode with the first radial mode will be selected. This is consistent with experimental observations and our $Fr = \infty$ results. The analysis of Sipp & Jacquin (2003) gives the corresponding wavenumber and growth rate as $ka = 2.26$ and $\sigma^* = 1.38$, respectively. LW98 report $ka = 1.6 \pm 0.2$ and $\sigma^* = 0.94$.

As discussed in Sipp & Jacquin (2003), viscosity will not only reduce the perturbation growth rate, but also increase the vortex radius, a, and hence a/b. The diffusive growth of an Oseen vortex, with the scaling defined in § 2, can be expressed as,

$$\left(\frac{a}{b_0}\right)^2 = \left(\frac{a_0}{b_0}\right)^2 + \frac{8\pi t^*}{Re_\Gamma}, \tag{3.9}$$

where $t^* = t\Gamma/(2\pi b_0^2)$ is non-dimensional time. Using (3.9) and data from LW98, the change in a/b in their experiments can be estimated. As stated earlier, at the start of their experiments, $a/b = 0.15$. For the time interval over which their σ^* is evaluated (see figure 14*b* in LW98), a/b varies in the range $0.24 < a/b < 0.31$. Thus, a/b increases by approximately 33 % during this time and by 100 % during the evolution from initial generation through the linear phase. As discussed by Sipp & Jacquin (2003), simply rescaling the wavenumber with an appropriate a will not account for the difference between the predicted $ka = 2.26$ and measured $ka = 1.6$ (e.g. $ka = kb \times a/b = 8.16 \times 0.24 = 1.96$).

Sipp & Jacquin (2003) also performed a linear stability analysis which accounts for the effects of viscosity on both the perturbation field and the base flow radius, $a = a(t)$. In this case, the perturbation growth rates depend on Re_Γ, kb and a/b. Since a/b now varies in time, the growth rates for each kb also vary in time. The solution is determined by integrating in time a non-autonomous amplitude equation. Results are obtained for $Re_\Gamma = 2750$ in order to match LW98. The growth rate corresponding to the wavenumber $kb = 8.16$ of LW98 is determined to be $\sigma^* = 0.99$ which agrees well with the value $\sigma^* = 0.94$ determined by LW98. In general, since the kb dependency of the growth rate develops in time, the wavenumber associated with the maximum growth rate and the wavenumber bands associated with the radial modes are no longer explicitly indicated. Although the analytical results indicate a wavenumber near $kb = 8.16$ with a local maximum growth rate, wavenumbers $kb > 8.16$ appear to have comparable growth rates and initiate growth earlier in time. The determination of which kb is selected is not clear.

In regards to our $Fr = \infty$ results, for which $Re_\Gamma = 2400$, the most amplified wavenumber is found to be $k_{max}b_0 = 6.3$ (with some uncertainty associated with the finite domain) and the corresponding growth rate is $\sigma^* = 0.83$. The lower $k_{max}b_0$ and σ^* are consistent with the lower Re_Γ. Using (3.9), we estimate for the linear phase ($3.4 < t^* < 12.0$ over which σ^* is determined) a range of a/b values, $0.23 < a/b < 0.38$. The values are comparable to the values in LW98. However, since the wavelength and growth rates are time dependent, there may be greater sensitivity to initial conditions and this is what we observe in our simulations. With these considerations, the differences between our results and those of LW98 are reasonable.

We now consider the effects of stratification in which both a and b may vary. In the case of weak to moderate stratification ($Fr \geqslant 2$), the most amplified wavelength is the same as that of the unstratified flow, i.e. $k_{max}b_0 = 6.3$. However, as indicated in table 1, σ^* increases with increasing stratification. Under these conditions, stratification does not significantly affect the vortex radius, a, but does affect the vortex separation, b, as indicated in figure 12(*a*). Thus, if the wavenumber scales with a, but growth rates vary with a/b, we expect the observed behaviour. While viscosity acts to increase a, stratification causes a reduction in b, thereby enhancing the increase of a/b in time. For the Fr range considered, the reduction in b increases with increasing stratification. For $Fr = 2$, using (3.9) to estimate the variation of a and results from figure 12(*a*) to evaluate b, we obtain a range of values, $0.19 < a/b < 0.53$ for the estimated duration of the linear phase ($2 < t^* < 5.25$). Although both viscosity and stratification act to increase a/b, the physical effects on the perturbation field differ. While viscosity acts to damp the growth of the perturbations, the reduction in b caused by stratification results in an enhanced amplification of the perturbations. It should be noted that even in unstratified flow, a smaller b results in greater amplification of the perturbations. Details of the variation of the growth rate with b will be discussed below.

In the strongly stratified flow ($Fr = 1$), the first radial mode is associated with a higher wavenumber $k_{max}b_0 = 8.4$ than in the unstratified flow. As indicated in figures 18 and 26, the vortices are in close proximity and exhibit smaller radii. If we assume that the axial wavelength of the maximum growth rate scaled with a is fixed at $ka = 2.26$, k must increase if a decreases. Viscous results for Sipp & Jacquin (2003) do show that the growth rate peaks at higher kb for lower a/b (see figure 9*b* in Sipp & Jacquin 2003). Additionally in the $Fr = 1$ flow, the second radial mode is also present. According to inviscid theory for unstratified flow, this must be associated with the higher axial mode, $kb_0 = 10.5$. The reason why this mode is amplified enough to become visible is not clear. The inviscid analysis of Sipp & Jacquin (2003) indicates that for $a/b = 0.288$, the first radial mode dominates. However, for lower a/b ($a/b = 0.208$), the analysis indicates that the growth rate of the second radial mode slightly exceeds ($\sigma^* = 1.39$) that of the first radial mode ($\sigma^* = 1.38$). In our $Fr = \infty$ flow, $a/b = 0.23$ at the start of the linear phase and increases in time owing to viscous effects. Thus, according to inviscid theory, significant development of the second radial mode will not occur. Since a/b increases in time in the weak to moderately stratified flows, we expect similar behaviour. For the $Fr = 1$ flow, an estimate of $a/b = 0.15$ is obtained for the start of the linear phase ($t^* = 1$). Since both a and b decrease in this flow, a/b will not significantly increase as in the $Fr \geqslant 2$ flows. For the lower a/b, it is possible that the growth rate of the second radial mode is significant enough to develop in the flow. The viscous analysis of Sipp & Jacquin (2003) does not consider additional radial modes, although it does indicate an earlier growth of higher kb (e.g. $kb_0 = 10$). As indicated earlier, we do observe comparable growth rates for wave modes in the range $6\pi/3 \leqslant kb_0 \leqslant 10\pi/3$. Although we expect viscosity to damp the growth rates of high wavenumbers, the $Fr = 1$ flow exhibits a shorter adjustment phase and higher growth rates, which may minimize damping and allow the selection of higher wave modes. In general, stratification effects are significant in this flow and we should not expect existing stability results to apply. In addition to changes in a and b, the vortices are no longer elliptical or Gaussian. The base flow changes significantly in time and we may be observing the corresponding changes and/or competition in instability modes.

The increased growth rates in the stratified flows can be explained physically by the reduction in the vortex separation, b, which enhances the strain in the vortices. Figure 19 shows cross-sections of the vortex pair indicating the local structure of the flow for $Fr = \infty$ and $Fr = 2$. Superimposed on contours of axial vorticity magnitude ω_y (grey shading) are instantaneous streamlines (black lines) and vectors indicating the magnitude and direction of the eigenvectors of the principal extensional strain, α. The vectors are scaled to the same length in both flows, thus indicating an enhancement of strain in the stratified flow (figure 19*b*).

According to elliptic instability theory (Waleffe 1990), the growth rate is proportional to the strain rate. For a vortex pair, the growth rate is typically non-dimensionalized with the external strain, $\Gamma/2\pi b_0^2$, which is the strain induced by one vortex at the centre of the other if that vortex is not there. The actual strain near the core centre is $\Gamma/\pi b^2$, i.e. the internal strain (LW98; Sipp & Jacquin 2003). From the DNS results, we evaluate directly the principal extensional strain, α, at the vortex centre (axial average). Figure 20(*a*) shows the time development of α normalized by its inital value, α_0. Initially, the value of α corresponds to that of the external strain, i.e. $\alpha_0 = \Gamma/2\pi b_0^2$. However, the results show that α quickly attains the value expected for the internal strain and thus $\alpha/\alpha_0 \approx 2$. This is in agreement with the results of Sipp & Jacquin (2003) who show the behaviour of $|\boldsymbol{S}|$ for the

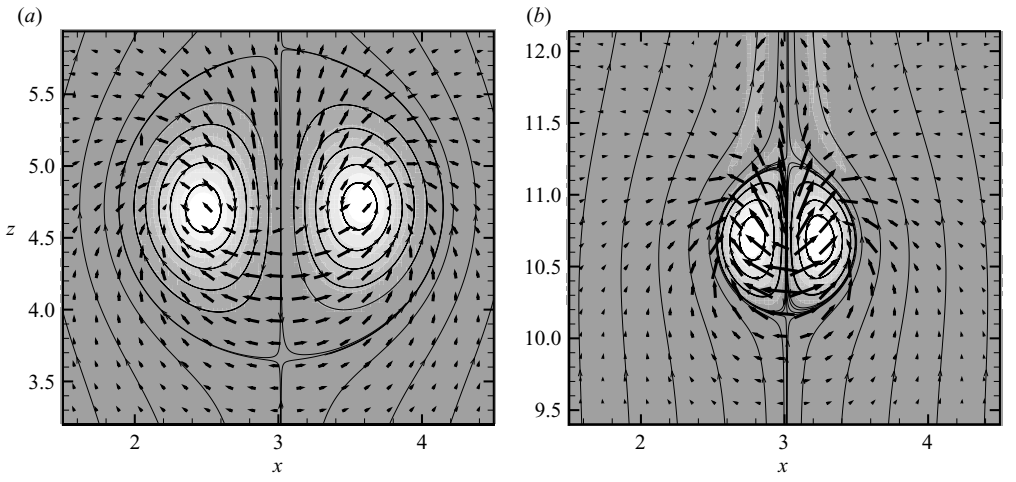

FIGURE 19. Cross section of the vortex pair for (*a*) $Fr=\infty$, $t^*=12.0$, (*b*) $Fr=2$, $t^*=5.25$. Grey shading, solid black lines and arrows show axial vorticity, instantaneous streamlines and vectors indicating direction and magnitude of principal extensional strain, respectively.

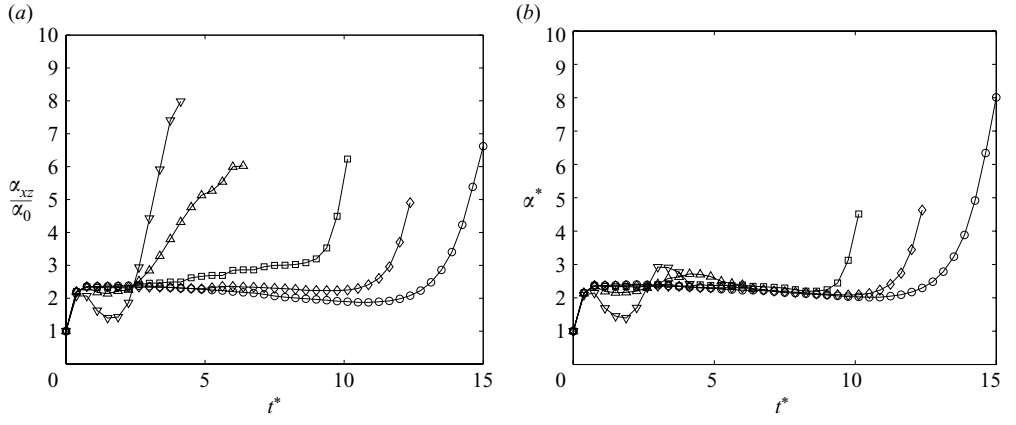

FIGURE 20. Principal extensional strain at vortex centre. (*a*) Magnitude normalized by initial value, α/α_0, (*b*) magnitude normalized by estimated external strain, $\alpha^*=(\alpha/\alpha_0)/(\Gamma/2\pi b^2)=(\alpha/\alpha_0)/(W_0/b)\approx(\alpha/\alpha_0)(b/b_0)$. Symbols: ○, $Fr=\infty$; ◇, $Fr=10$; □, $Fr=5$; △, $Fr=2$; ▽, $Fr=1$.

two-dimensional Lamb–Oseen dipole. For $Fr=\infty$, there is a steady decline in α before a rapid increase near the end of the linear phase. Note that the increase occurs at the same time as the corresponding eigenvector indicates a directional change (figure 14*a*). With weak to moderate stratification, there appears to be a compensating enhancement in α which increases with increasing stratification. Comparison with figure 12(*a*) suggests a direct correspondence between separation distance reduction and strain rate enhancement. A normalized strain is defined here as,

$$\alpha^* = \frac{\alpha}{\Gamma/2\pi b^2} \approx \frac{\alpha}{W_0/b} = \frac{\alpha/\alpha_0}{b_0/b}, \tag{3.10}$$

where $W=\Gamma/2\pi b$ is taken to be constant as indicated by the simulation results (see figure 11, $Fr>2$). Figure 20(*b*) shows the time development of α^*. For weak stratification, the curves collapse onto that of the unstratified flow suggesting that

the strain rate is not distinctly altered by stratification, but only enhanced through a reduced separation distance. For $Fr \leqslant 2$, however, the effects of stratification are significant and change the behaviour of the strain rate. In fact, for $Fr = 1$, the strain rate shows a decrease at the onset of the instability. This may explain the changing trends in σ^* for $Fr = 1$ (table 1).

We can consider a modified non-dimensional growth rate, σ_b^*, which accounts for the change in b,

$$\sigma_b^* = \frac{\sigma}{W_0/b}, \tag{3.11}$$

where b is a representative value during the time interval that σ is evaluated. The results are given in table 1. Values of σ_b^* for weak to moderately stratified flows ($10 \geqslant Fr > 2$), are comparable to that of the unstratified flow. However, for strong stratification ($Fr < 2$), σ_b^* actually decreases.

We now consider the results reported by Delisi & Robins (2000). Recall that they peformed both experiments ($Re_\Gamma = 24\,000$) and simulations ($Re_\Gamma = 1465$) with Fr ranging from 0.73 to 1.10; thus, our strongly stratified flow ($Re_\Gamma = 2400$, $Fr = 1$) falls within their range of flow conditions. Our results are consistent with their qualitative observations of an earlier onset and more rapid growth of the instability in the stratified flows. However, they observe longer wavelengths ($1 \leqslant \lambda/b_0 \leqslant 2$) than in the unstratified flows ($\lambda/b_0 \leqslant 1$). They also observe the wavelength increasing in time, which is not indicated in the present results. The reasons for these differences are not clear. Delisi & Robins (2000) indicate an initial vortex radius of $0.16b_0$ in their simulations and smaller radii in their experiments. A smaller a would, however, produce shorter wavelengths and thus does not explain the observed difference with our results. Since $Re_\Gamma = 24\,000$ in their experiments, the differences should not be attributed to viscous effects. In comparing their simulations with those of the present study, a key difference is their axial domain length which is $10b_0$. This allows the development of the Crow instability which may influence the short-wavelength instability and in particular, modify the development of the wavelength. Another, related, difference is their initialization of the perturbation field which consists of a superposition of sinusoidal deformations of the vortices. The axial phase of each mode is random and the wavenumbers include the low-frequency range, which is not included in our simulations owing to the shorter axial length. These additional modes could develop, at a slower rate, and interact with the short wave, resulting in their growth. In their experiments, although the development of the Crow instability was not observed, it is likely that the associated modes are present and growing in time. In addition, the range of Fr considered in their study, 0.73–1.10, includes $Fr < 1$ which represents very strong stratification. At Fr less than some critical value, Fr_{cr} (where $Fr_{cr} < 1$), the separation distance increases and the flow behaves fundamentally differently (Mahoney 2002). Thus, $Fr \sim 1$ may correspond to the transition between two distinct flow regimes. As indicated by our results, $Fr = 1$ shows significantly different characteristics from those in the unstratified and moderately stratified flows. The condition of $Fr \sim 1$ along with the possible presence of the Crow instability may have caused the short-wave instability to be susceptible to variation in their flows.

In summary, the present results show that in the case of weak to moderate stratification ($\infty > Fr \geqslant 2$), the elliptic short-wave instability is exhibited and fundamentally similar to that in unstratified flow. In this case, the time scale of buoyancy is greater than that of the flow instability. Although stratification effects are present, they do not interact significantly with the instability. The principal effect is to reduce the

separation distance which enhances the strain rate thereby increasing the growth rate of the instability. This is consistent with linear stability theory for unstratified flow. In the case of strong stratification ($Fr = 1$), the time scale of buoyancy is comparable to that of the instability. The effects of stratification interact significantly with the instability growth. The two-dimensional base flow changes considerably and alters the three-dimensional development of the flow.

3.4. *Nonlinear phase*

We now consider the development of the flow during the nonlinear phase in which the perturbation amplitudes are significant and, as seen in the flow visualizations (figures 2–4), secondary structures are formed which lead to the breakdown of the vortex pair.

In the unstratified flow, the early stage of the nonlinear phase is marked by the formation of 'knobs' which appear at the peaks of the sinusoidal deformation (figure 2*c*, $t^* = 13.5$). Vorticity concentrates within the knobs as indicated at the subsequent time (figure 2*d*, $t^* = 15.0$). Transverse secondary structures develop at the leading edge, i.e. the bottom of the descending vortex pair oval, and eventually dominate the flow (figure 2*e*, *f*, $t^* \geqslant 16.5$). These structures consist primarily of transverse vorticity, ω_x. During this time period, the vortex circulation Γ (figure 7*a*), exhibits an enhanced decay while the perturbation energy spectrum shows the development of harmonics of the primary instability (figure 15*a*).

As discussed in LW98, the formation of these structures is explained by considering the distinct geometry of the cooperative elliptic instability which brings the primary vortices closer together at the leading edge of the vortex pair (see figure 13*c*). As discussed in § 3.3, the phase relationship of the deformation is such that inner and outer layers of a vortex are displaced in opposite directions. Figure 21(*a*) is an enlarged view of figure 13(*a*) which clearly shows the relative deformation of the inner core and outer layer of each vortex. Figure 22(*a*) depicts, at the same instant in time, a vertical slice through the centre of one of the vortices. The plot shows contours of transverse vorticity ω_x. Note that with respect to this particular plane, ω_x essentially corresponds to the azimuthal vorticity of the vortex which exhibits this characteristic structure (see figure 12 in LW98). The centre row of alternating signed ω_x, corresponds to the deformation of the primary core. Above and below this is a row of alternating signed ω_x, corresponding to the deformation of the outer layer. At a given axial location, the ω_x in the outer layer is of opposite sign to that in the core consistent with the respective phase relationship. As the outer layers of one vortex come into close proximity with the inner core of the other at the leading edge, fluid is extracted from one vortex into the other (LW98). This is shown in figure 21(*b*) (see also figure 25*b*). The transverse vorticity within the outer layer is thereby stretched and amplified as indicated in figure 22(*b*) which shows enhanced ω_x in the bottom row (leading edge). Subsequently, ω_x becomes the dominant component of vorticity and the resulting structure extends over the leading edge of the vortex pair oval (figure 2*e*, $t^* = 16.5$). An array of transverse counter-rotating vortex pairs results, two pairs for every wavelength of the primary instability (one pair from each vortex – see figures 21*b* and 22*b*), in agreement with the experimental observations of LW98.

For times $t^* > 15$, figure 15 indicates a broadening of the spectrum. The high-wavenumber modes are no longer distinct, indicating the development of a small-scale structure. Eventually, the primary instability becomes saturated and the corresponding growth rate is reduced to zero. At $t^* = 18.0$, the corresponding energy spectrum (figure 15*a*) is quite broad with no preferred mode, although coherent structures remain in the flow (figure 2). Evidently, there is sufficiently complex small-scale

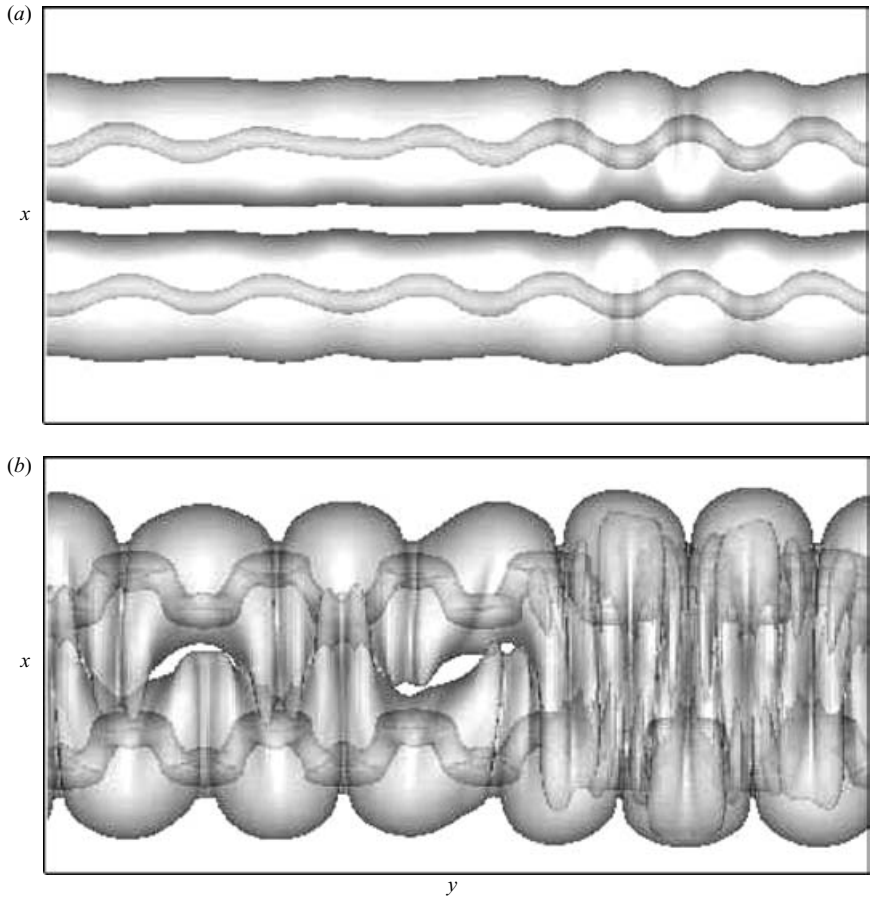

FIGURE 21. Bottom view of vortex pair for $Fr = \infty$ showing isosurfaces of high and low vorticity magnitude at (*a*) $t^* = 12.0$ and (*b*) $t^* = 15.0$.

structure and effective energy transfer across all modes. Laporte & Corjon (2000) suggest that transition to turbulence occurs when all modes have reached the same order of magnitude and all growth rates are zero or less. Late-time spectra ($t^* > 18.0$, not shown) for the present results do indicate growth rates of zero or less for all modes.

In weakly to moderately stratified flows, knob structures also form (figure 3*c*, $Fr = 5$ at $t^* = 9.75$; figure 4*b*, $Fr = 2$ at $t^* = 6.0$). The corresponding energy spectra (figures 15*b*, *c*) show the development of harmonics. The extraction of outer layer fluid from one vortex into the other at the leading edge of the vortex pair also occurs and transverse structures are exhibited in the weakly stratified flow ($Fr = 5$, figure 3*e*, $t^* = 11.25$). However, in the moderately stratified flow ($Fr = 2$, figure 4), the transverse structures no longer dominate. This is due to the deceleration of the vortex pair descent caused by baroclinic torque which results in a reduced extensional strain at the leading edge. Consequently, amplification of ω_x at the leading stagnation point is not as significant. Alternatively, pairs of counter-rotating vertical structures develop, between and above the primary vortices, with one pair for every wavelength of the primary instability (figure 4, $t^* = 6.75$). Such vortex structures were observed in the simulation results of Delisi & Robins (2000) and Holzäpfel *et al.* (2001). These structures are dominated by vertical vorticity, ω_z.

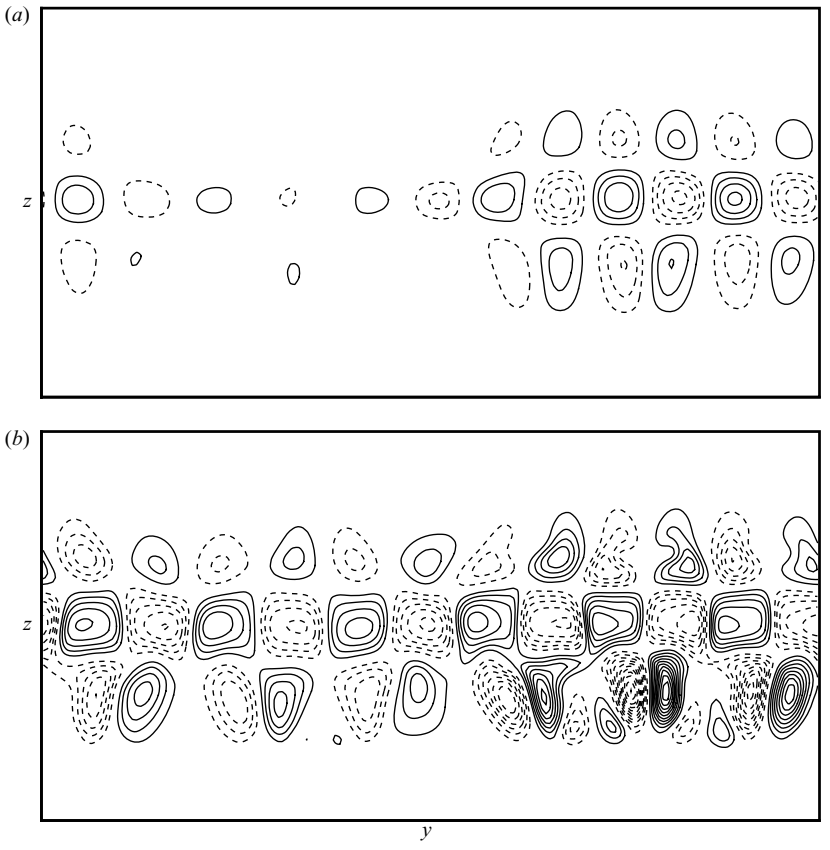

FIGURE 22. Vertical slice through one vortex core showing contours of transverse vorticity, ω_x, associated with the deformation of inner core and outer layer for $Fr = \infty$. (*a*) $t^* = 12.0$, Contour level increments $\Delta\omega_x/\omega_{yo} = \pm 0.0125$. (*b*) $t^* = 15.0$, Contour level increments $\Delta\omega_x/\omega_{yo} = \pm 0.025$.

Figure 23(*a*) shows contours of vertical vorticity, ω_z, in a horizontal slice ((x, y)-plane) through the vortex pair in the unstratified flow. Analogous to figure 22, ω_z effectively corresponds to the azimuthal vorticity with respect to this particular plane. There are two rows of alternating signed ω_z corresponding to the deformation of the two primary vortex cores. On either side of each core is a row of alternating signed ω_z corresponding to the deformation of the outer layers. Figure 23(*b*) shows the corresponding plot for the moderately stratified flow, $Fr = 2$. Owing to the reduced separation distance, the outer layers with like-signed vorticity overlap in between the cores, resulting in locally enhanced ω_z (at the end of the linear phase, ω_z is approximately twice the magnitude of that in the outermost rows). Figure 24 displays vertical slices ((x, z)-plane) of the vortex pair showing vorticity magnitude (contour levels) and the magnitude and orientation of the principal extensional strain (vectors). In the unstratified flow (figure 24*a*), there is no significant stretching in the vertical direction between the vortices and thus, there is no significant development of ω_z and associated vertical structures. In the stratified flow (figure 24*b*), there is significant vertical strain between and above the vortices. The already enhanced ω_z thereby becomes further amplified. The vertical strain is due to both the reduced separation distance and the baroclinically generated secondary vortices which pulls fluid upward

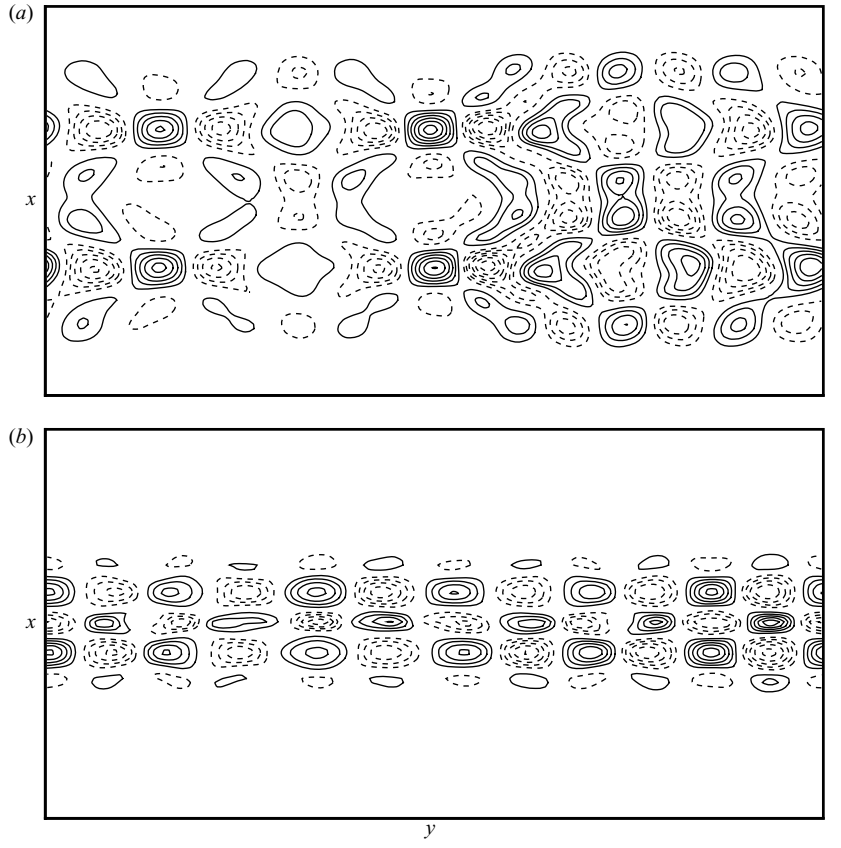

FIGURE 23. Horizontal slice through vortex pair showing contours of vertical vorticity, ω_z, associated with the deformation of inner cores and outer layers for (*a*) $Fr = \infty$, $t^* = 12.0$ and (*b*) $Fr = 2$, $t^* = 5.25$. Contour level increments $\Delta\omega_x/\omega_{y0} = \pm 0.005$.

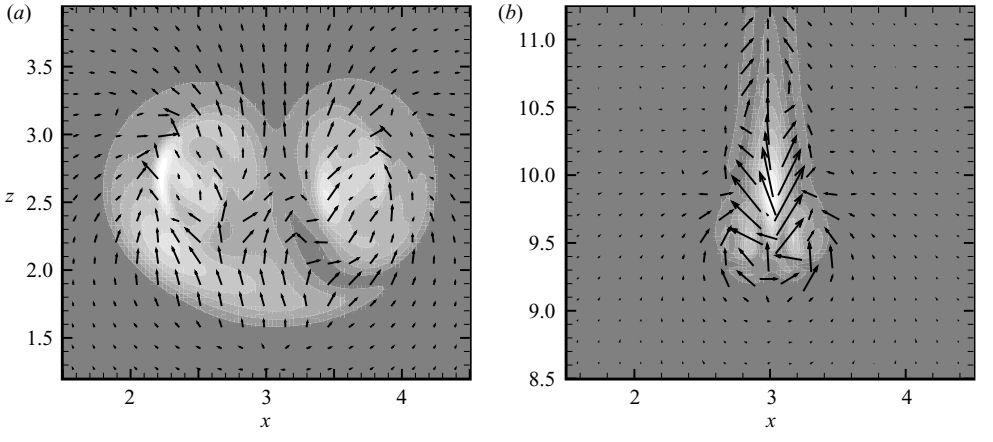

FIGURE 24. Cross-section of the vortex pairs. Grey shading shows the vorticity magnitude with maximum vorticity shaded white, and vectors show direction and magnitude of extensional strain in the (x, z)-plane. Length of vectors are equally scaled; longer vertical vectors in (*b*) indicates significant enhancement of the principal extensional strain in-between and inside the vortex cores. (*a*) $Fr = \infty$, $t^* = 15.0$. (*b*) $Fr = 2$, $t^* = 6.75$.

from the trailing edge, i.e. the top of the descending vortex pair oval (see figure 25*e*). This leads to the formation of downstream vertical structures in the $Fr = 2$ flow. By $t^* = 7.5$ (figure 4*d*), ω_z is the dominant component of vorticity in the flow. In the case of weak stratification ($Fr = 5$, figure 3), the transverse and vertical structures are comparable in strength and both are observed in the flow.

The development of these vertical structures was discussed by Holzäpfel *et al.* (2001). Their results indicate that the opposite signed baroclinically generated ω_y surrounding the vortex pair is influenced by the short-wave instability resulting in rib-like structures near the trailing edge. It was suggested that these structures induce a transverse velocity field, u, with high gradients in the axial direction, $\partial u/\partial y$, thereby establishing ω_z. The ω_z is then amplified through vortex stretching caused by the accelerating downward motion between the primary vortices. Their analysis, however, did not consider the distinct geometry of the cooperative elliptic instability which controls the development of the transverse secondary structures in the unstratified flow. Our results indicate that the ω_z associated with the vertical structures originates as azimuthal vorticity in the outer layers which is intrinsic to the primary instability and not particular to stratification as suggested in Holzäpfel *et al.* (2001). The effects of the baroclinic vorticity which do promote ω_z are indirect: the reduced vortex separation causes merging of the outer layers in between the vortices and the induced flow at the trailing-edge region establishes an enhanced vertical strain.

The spectrum corresponding to the $Fr = 2$ flow (figure 15*c*, $t^* = 6.75$) exhibits the development of the first harmonic. Beyond this time, the primary mode saturates and the spectrum broadens at the high wavenumbers. The peaks associated with the primary mode and first harmonic tend to persist owing to the generated baroclinic torque which persists downstream of the vortex pair. Although the spatial structure at this late stage differs significantly between the unstratified and weak to moderately stratified flows, the behaviour of the energy spectrum is otherwise generally similar.

The implication of the different secondary structures in the unstratified and moderately stratified flows on the breakdown process is now considered. Figure 25 shows contours of axial vorticity, ω_y, in a vertical slice ((x, z)-plane) at several times for the unstratified and stratified ($Fr = 2$) flows. In the unstratified flow, the extraction of fluid from one vortex to the other (figure 25*b*) brings vorticity of opposite sign in close proximity (figure 25*c*). This mechanism of fluid exchange in the transverse direction promotes mixing and decay of the vortices (LW98). In the stratified flows, this mechanism also occurs to varying degree, depending on the level of stratification. In the $Fr = 2$ flow, as indicated in figure 25(d, e), positive axial vorticity originating from the left-hand vortex is seen to occur on the right-hand side near the leading edge. However, the presence of counter-rotating vertical structures enables an additional mechanism of fluid exchange in the transverse direction. This is observed in figure 25*f* which shows positive axial vorticity originating from the left-hand vortex on the right-hand side near the trailing edge. In addition, there is detrainment of the primary vortices at the trailing edge by the secondary baroclinic vortex structures. These additional mechanisms of vortex breakdown result in a more rapid decay of the vortex pair in the stratified flows (figure 10).

In the case of strongly stratified flow ($Fr = 1$), the primary vortices decay significantly during the linear phase. As discussed earlier, the time scale of buoyancy is comparable to that of the instability and significant interaction is observed. Figure 26 shows time sequences of (x, z)-plane contours of temperature, T, and axial vorticity, ω_y; the times correspond to those of the three-dimensional visualizations in figure 5. As indicated in the plots, the effects of baroclinic torque are so significant that they eventually

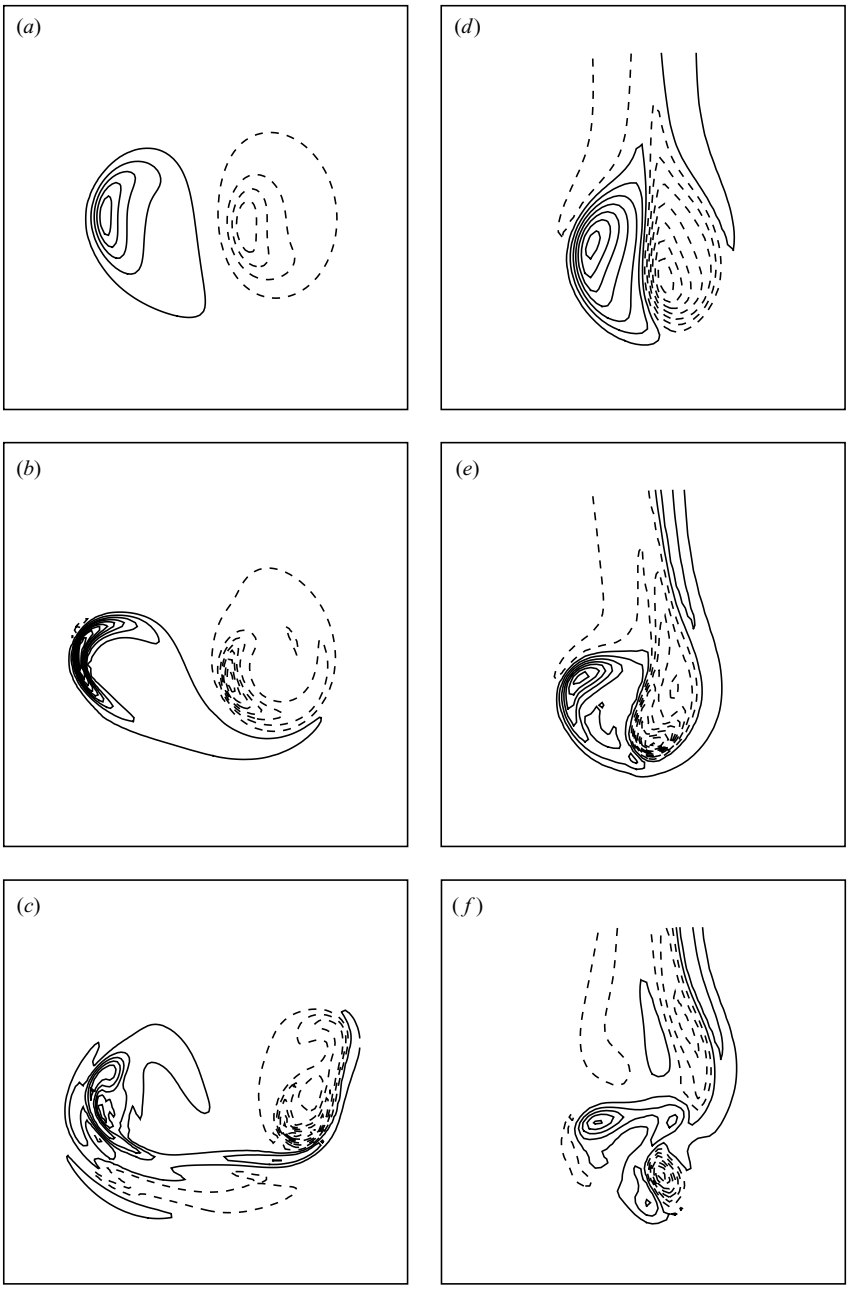

FIGURE 25. Contours of axial vorticity, ω_y, in (x, z)-plane for (a)–(c) $Fr = \infty$ at $t^* = 13.5, 15.0, 16.5$ and (d)–(f) $Fr = 2$ at $t^* = 6.0, 6.75, 7.5$ (solid line: $\omega_y > 0$, dashed line: $\omega_y < 0$).

dominate the flow. At early times ($t^* \leqslant 4.5$, linear phase), as a result of these effects, the primary vortices are brought together and interdiffuse. In addition, there is detrainment of the primary vortices at the trailing edge. These mechanisms result in rapid decay of the primary vortex pair (figure 10) before significant development of the three-dimensional instability and associated secondary structures (figure 5*a*, *b*). At subsequent times, there is some indication of the secondary vertical structures

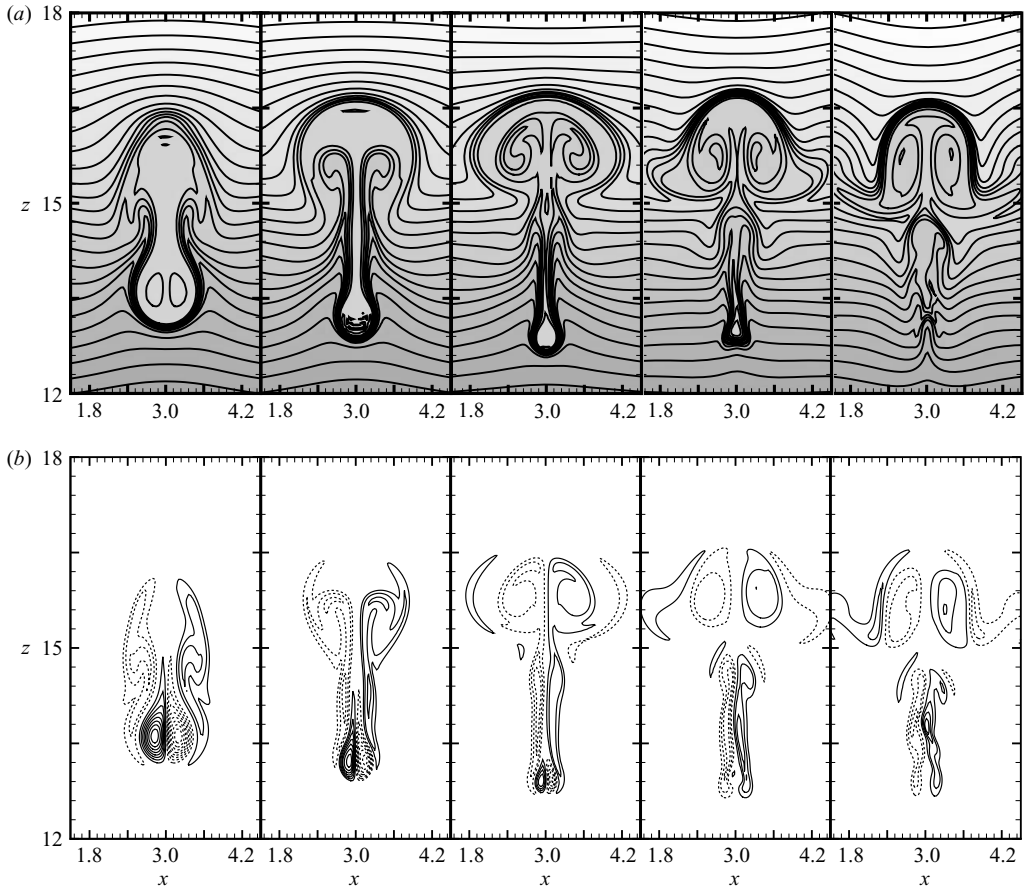

FIGURE 26. Cross-section showing contours of (*a*) temperature, $\widetilde{T}$, and (*b*) axial vorticity, ω_y, for $Fr = 1$ at $t^* = 3.75, 4.5, 5.25, 6.0, 6.75$ (from left to right). Contour levels at $\Delta\widetilde{T}/\Delta\overline{T} = 0.5, 1.0, 1.5$, etc. and $\Delta\omega_y/\omega_{ymax}(t^* = 0) = \pm 0.05, \pm 0.1$, etc. (where $\Delta\overline{T} = b_0 \mathrm{d}\overline{T}/\mathrm{d}z$). Contours with negative value are indicated by dashed lines.

associated with the original vortex pair (figure 5*c*, $t^* = 5.25$). At the same time, as the baroclinically generated vorticity moves upwards, it advects heavier fluid into regions of light fluid (figure 26*a*). This leads to secondary baroclinic torque which is of opposite sign to the preceding baroclinic vorticity. This process of successive generation of opposite signed baroclinic torque occurs at the buoyancy period $Nt = 2\pi$, which corresponds to the observed oscillation in Γ of figure 7(*b*). In fact, these results indicate that moderately stratified flows ($2 \leqslant Fr \leqslant 5$) eventually become buoyancy dominated once the primary vortex pair decays. At very late times, internal waves dominate the $Fr = 1$ flow and, as discussed in §§ 2 and 3.2, the influence of the image vortices resulting from the periodic boundary conditions are no longer negligible. The internal waves generated by the periodic array of vortices establish a standing wave pattern near the buoyancy frequency (figure 7*b*).

The baroclinic vorticity structures are themselves influenced by the elliptic instability (see middle region of figure 5*d*, $t^* = 6.0$ and compare, e.g. with figure 4*b*). The corresponding spectra (figure 15*d*) shows some indication of the first harmonic. As in the other cases, the primary mode saturates and the spectrum broadens at the high

wavenumbers. The primary mode peak persists throughout the times shown in figure 5. We also observe evidence of the two-dimensional instabilities reported by Garten *et al.* (1998). One instability, which Garten *et al.* refer to as the 'vortex head instability', is associated with the primary vortex pair which exhibits sinusoidal motion as it propagates. This is a result of preferential detrainment of the primary vortices by the baroclinic torque which alternates from one vortex to the other. There is some indication of this in our $Fr = 2$ flow (figure 25*d*–*f*). The other instability is a jet instability of the baroclinically generated vorticity (which corresponds to a jet flow). In the strongly stratified flow $Fr = 1$, there is some indication of a sinuous mode in the vertical vortex structures at the later times (figure 26*b*, $t^* = 6.75$). Both of these instabilities result in asymmetry in the two-dimensional flow (Garten *et al.* 1998).

4. Conclusions

The effects of stable stratification on the development of the short-wavelength instability and subsequent decay of a counter-rotating vortex pair have been investigated using direct numerical simulations. A range of Froude numbers, $1 \leqslant Fr \leqslant \infty$, is considered. A more quantitative assessment of the flow is carried out than in previous studies. Depending on the level of stratification, as characterized by Fr which indicates the ratio of the time scale of buoyancy to that of the instability, and the stage of evolution, stratification effects may significantly alter the behaviour of the flow. The evolution of the flow is described in terms of the adjustment phase, in which the vortices adjust to the presence of each other and develop a mutually induced strain field, the linear phase, in which perturbation amplitudes grow and the instability develops, and the nonlinear phase, in which perturbation amplitudes are significant and secondary vortex structures dominate the flow. This study considers the linear and nonlinear phases where three-dimensional effects are significant.

In the linear phase of evolution, the vortex pair in unstratified fluid ($Fr = \infty$) exhibits the elliptic short-wavelength instability with characteristics and behaviour in agreement with the experiments of LW98.

In weak to moderately stratified flows ($\infty > Fr > 2$), in which the time scale of buoyancy is greater than that of the flow instability, the observed instability is fundamentally similar to that in unstratified flow. Although stratification effects are present, they do not affect the qualitative characteristics of the instability. The principal effect is to reduce the separation distance which enhances the induced strain, thereby increasing the growth rate of the instability. Consequently, the instability exhibits an earlier onset and higher growth rate with increasing stratification. The behaviour is essentially described by linear stability theory for unstratified flow if the varying separation distance is taken into account. Our analysis suggests the growth rate scaling as $\Gamma/2\pi b^2 = W_0/b$ where $b = b(t)$ is given by two-dimensional theory (Saffman 1972; Crow 1974).

In the case of strong stratification ($Fr = 1$), the time scale of buoyancy effects is comparable to that of the instability. The effects of stratification interact significantly with the development of the instability and alter its characteristics and behaviour. As a result of strong baroclinic torque, the primary vortices are brought together and interdiffuse. In addition, there is detrainment by the baroclinically generated vorticity. The associated reduction in radii of the vortices results in a higher axial wave mode and a more complex radial structure of the instability. Since the shape of the vortices is significantly altered, it may be that the observed instability can no longer be considered an elliptic instability.

Our results of an earlier onset and more rapid growth of the instability in the stratified flows is in agreement with previous studies (Delisi & Robins 2000; Holzäpfel *et al.* 2001). However, the longer wavelengths which increase in time, reported by Delisi & Robins (2000), are not consistent with our results. This may be due to the presence of the Crow instability in their flows. Additionally, the range of Fr considered in their study, $0.73-1.10$, may correspond to the transition between two distinct flow regimes. As indicated by our results, $Fr=1$ shows significantly different characteristics from those in the unstratified and moderately stratified flows. Detailed features such as the presence of the second radial mode would be difficult to determine experimentally. Further experiments over a greater range of Fr would be valuable.

Overall, our analysis of the linear phase provides more quantitative information than in previous studies of the short-wave instability in the presence of stratification. Although the behaviour of weak to moderately stratified flows can be explained using stability analysis results for unstratified flow, this is not the case for the strongly stratified flow. In general, a linear stability analysis is required to obtain accurate estimates of the growth rates and axial wavelengths of the fastest growing short-wave instabilities in stratified conditions. This requires an analysis of the type developed by Billant *et al.* (1999) and Sipp & Jacquin (2003), but generalized to include the effects of stratification. Such an analysis would have to account for the time-varying effects of both viscous diffusion, which acts to increase the size of the vortex radii and damp the perturbation growth rates, and stratification, which decreases the separation distance thereby amplifying growth rates and may also decrease the vortex radii. In this case, the reduction in vortex radii represents a combined effect of viscosity and stratification.

In the nonlinear phase of evolution, the early stages of development in unstratified and weak to moderately stratified flows are controlled by the distinct geometry of the short-wave instability. The phase relationship of the initial deformation results in periodic extraction of outer-layer fluid from one vortex into the other at the leading edge of the vortex pair. This initiates the vortex breakdown process in the unstratified flow. The azimuthal vorticity in the outer layers of the primary vortices are amplified owing to the extensional strain at the leading stagnation point and transverse secondary vortex structures are formed.

In weak to moderately stratified flows ($\infty > Fr \geqslant 2$), although buoyancy effects do not significantly alter the nature of the linear phase, they can dominate in the nonlinear and late stages of evolution. In these flows, vortex decay is enhanced owing to additional mechanisms not present in unstratified flow. The effects of baroclinic torque result in the amplification of azimuthal vorticity in between the primary vortices leading to the formation of vertical vortex structures. These structures provide an additional mechanism of fluid exchange in the transverse direction. Detrainment of the primary vortices by the generated baroclinic torque also contributes to the breakdown of the vortices. These additional mechanisms lead to a more rapid breakdown and decay of vortex pair.

In the case of strong stratification ($Fr=1$), the significant reduction in vortex separation along with detrainment, results in an accelerated decay of the primary vortices. Late-time evolution is dominated by the successive generation of alternate signed baroclinic torque which results in an oscillation of the total flow circulation at the buoyancy frequency.

The authors would like to acknowledge Julie Vanderhoff and Laura Brandt for their assistance with the numerical simulations. We also thank Professor Stefan Llewellyn Smith, Don Delisi and Bob Robins for helpful comments.

REFERENCES

Billant, P., Brancher, P. & Chomaz, J. 1999 Three-dimensional stability of a vortex pair. *Phys. Fluids* **11**, 2069–2077.

Crow, S. C. 1970 Stability theory for a pair of trailing vortices. *AIAA J.* **8**, 2172–2179.

Crow, S. C. 1974 Motion of a vortex pair in a stably stratified fluid. *Poseidon Research Report 1, Santa Monica, CA*, pp. 1–48.

Delisi, D., Greene, G., Robins, R., Vicroy, D. & Wang, F. 2003 Aircraft wake vortex core size measurements. *21st AIAA Applied Aerodynamics Conference, Orlando, Florida*, *AIAA*-2003-3811.

Delisi, D. P. & Robins, R. E. 2000 Short-scale instabilities in trailing wake vortices in a stratified fluid. *AIAA J.* **38**, 1916–1923.

Diamessis, P. J. & Nomura, K. K. 2000 Interaction of vorticity, rate-of-strain and scalar gradient in stratified homogeneous sheared turbulence. *Phys. Fluids* **12**, 1166–88.

Diamessis, P. J. & Nomura, K. K. 2004 The structure and dynamics of overturns in stably stratified homogeneous turbulence. *J. Fluid Mech.* **499**, 197–229.

Eloy, E. & Le Dizès, S. 1999 Three-dimensional instability of Burgers and Lamb–Oseen vortices in a strain field. *J. Fluid Mech.* **378**, 145–166.

Garten, J. F., Arendt, S., Fritts, D. C. & Werne, J. 1998 Dynamics of counter-rotating vortex pairs in stratified and sheared environments. *J. Fluid Mech.* **361**, 189–236.

Garten, J. F., Werne, J., Fritts, D. C. & Arendt, S. 2001 Direct numerical simulations of the Crow instability and subsequent vortex reconnection in a stratified fluid. *J. Fluid Mech.* **426**, 1–45.

Gerz, T., Schumann, U. & Elghobashi, S. 1989 Direct simulation of stably stratified homogeneous turbulent shear flows. *J. Fluid Mech.* **200**, 563–594.

Han, J., Lin, Y.-L., Schowalter, D., Arya, S. & Proctor, F. 2000 Large eddy simulation of aircraft wake vortices within homogeneous turbulence: Crow instability. *J. Aircraft* **38**, 292–300.

Holzäpfel, F. 2004 Adjustment of subgrid-scale parametrizations to strong streamline curvature. *AIAA J.* **42**, 1369–1377.

Holzäpfel, F. & Gerz, T. 1999 Two-dimensional wake vortex physics in the stably stratified atmosphere. *Aerosp. Sci. Technol.* **5**, 261–270.

Holzäpfel, F., Gerz, T. & Baumann, R. 2001 The turbulent decay of trailing vortex pairs in stably stratified environments. *Aerosp. Sci. Technol.* **5**, 95–108.

Jimenez, J., Wray, A. A., Saffman, P. G. & Rogallo, R. S. 1993 The structure of intense vorticity in isotropic turbulence. *J. Fluid Mech.* **255**, 65–90.

Laporte, F. & Corjon, A. 2000 Direct numerical simulations of the elliptic instability of a vortex pair. *Phys. Fluids* **12**, 1016–1031.

Laporte, F. & Leweke, T. 2002 Elliptic instability of counter-rotating vortices: experiment and direct numerical simulations. *AIAA J.* **40**, 2843–2494.

Leweke, T. & Williamson, C. H. K. 1998*a* Cooperative elliptic instability of a vortex pair. *J. Fluid Mech.* **360**, 85–119.

Leweke, T. & Williamson, C. H. K. 1998*b* Long-wavelength instability and reconnection of a vortex pair. In *Proceedings of the IUTAM Symposium on Dynamics of Slender Vortices*, pp. 225–234. Kluwer.

Mahoney, D. 2002 A numerical study of the effects of stratification on the short wave instability in a vortex pair. MS thesis, University of California, San Diego.

Meng, J. C. S. & Rottman, J. W. 1988 Linear internal waves generated by density and velocity perturbations in a linearly stratified fluid. *J. Fluid Mech.* **186**, 419–444.

Nomura, K. K. & Post, G. K. 1998 The structure and dynamics of vorticity and rate of strain in incompressible homogeneous turbulence. *J. Fluid Mech.* **377**, 65–97.

Orlandi, P., Carnevale, G. F., Lele, S. K. & Shariff, K. 1998 DNS study of stability of trailing vortices. In *Proceedings of the Summer Program 1998, Center for Turbulence Research*, pp. 187–208.

Robins, R. E. & Delisi, D. P. 1998 Numerical simulations of three-dimensional trailing vortex evolution in stratified fluid. *AIAA J.* **36**, 981–985.

Saffman, P. G. 1972 The motion of a vortex pair in a stratified atmosphere. *SIAM* **L1, 2**, 107–119.

Sarpkaya, T. 1983 Trailing vortices in homogeneous and density-stratified media. *J. Fluid Mech.* **136**, 85–109.

Sarpkaya, T. & Suthon, P. 1991 Interaction of a vortex couple with a free surface. *Exps. Fluids* **11**, 205–217.

Scorer, R. S. & Davenport, L. J. 1970 Contrails and aircraft downwash. *J. Fluid Mech.* **43**, 451–464.

She, Z.-S., Jackson, E. & Orszag, S. A. 1991 Structure and dynamics of homogeneous turbulence: models and simulations. *Proc. R. Soc. Lond.* A **434**, 101–124.

Sipp, D. & Jacquin, L. 2003 Widnall instabilities in vortex pairs. *Phys. Fluids* **15**, 1861–1874.

Spalart, P. R. 1996 On the motion of laminar wing wakes in a stratified fluid. *J. Fluid Mech.* **327**, 139–160.

Spalart, P. R. 1998 Airplane trailing vortices. *Annu. Rev. Fluid Mech.* **30**, 107–138.

Switzer, G. & Proctor, F. 2000 Numerical study of wake vortex behavior in turbulent domains with ambient stratification. *38th Aerospace Sciences Meeting & Exhibit, Reno, NV, AIAA* 2000-0755.

Thomas, P. J. & Auerbach, D. 1994 The observation of the simultaneous development of a long- and a short-wave instability mode on a vortex pair. *J. Fluid Mech.* **265**, 289–302.

Tsai, C.-Y. & Widnall, S. E. 1976 The stability of short waves on a straight vortex filament in a weak externally imposed strain field. *J. Fluid Mech.* **73**, 721–733.

Tsutsui, H. 2003 Evolution of a counter-rotating vortex pair in a stably stratified fluid. MS thesis, University of California, San Diego.

Waleffe, F. 1990 On the three-dimensional instability of strained vortices. *Phys. Fluids* A **2**, 76–80.